



Advancements in osmosis- and pressure driven membrane separation processes - Optimizations of membrane module designs through computational fluid dynamics

Aschmoneit, Fynn Jerome

Link to article, DOI:

<https://doi.org/10.11581/DTU:00000113>

Publication date:

2020

Document Version

Publisher's PDF, also known as Version of record

[Link back to DTU Orbit](#)

Citation (APA):

Aschmoneit, F. J. (2020). *Advancements in osmosis- and pressure driven membrane separation processes - Optimizations of membrane module designs through computational fluid dynamics*. Technical University of Denmark. <https://doi.org/10.11581/DTU:00000113>

General rights

Copyright and moral rights for the publications made accessible in the public portal are retained by the authors and/or other copyright owners and it is a condition of accessing publications that users recognise and abide by the legal requirements associated with these rights.

- Users may download and print one copy of any publication from the public portal for the purpose of private study or research.
- You may not further distribute the material or use it for any profit-making activity or commercial gain
- You may freely distribute the URL identifying the publication in the public portal

If you believe that this document breaches copyright please contact us providing details, and we will remove access to the work immediately and investigate your claim.

Advancements in osmosis- and pressure driven membrane separation processes

- Optimizations of membrane module
designs through computational fluid
dynamics

Fynn Jerome Aschmoneit

PhD Thesis
January, 2020

DTU Environment
Technical University of Denmark
Department of Environmental Engineering

Advancements in osmosis- and pressure driven membrane separation processes

- Optimizations of membrane module designs through computational fluid dynamics

Fynn Jerome Aschmoneit

PhD Thesis, January, 2020

The synopsis part of this thesis is available as a pdf-file for download from the DTU research database ORBIT: <http://www.orbit.dtu.dk>

Address: DTU Environment
Department of Environmental Engineering
Technical University of Denmark
Bygningstorvet, Building 115

Preface

This thesis is submitted in partial fulfillment of the requirements for the Degree of Doctor of Philosophy at the Department of Environmental Engineering at the Technical University of Denmark. The project was funded by the MEMENTO and NEPWAT projects, and conducted under supervision of Prof. Claus Hélix-Nielsen. The work was carried out at DTU Environment between January 2016 and January 2020. An intermediate employment at Aquaporin A/S between Mai 2018 and January 2019 was supported by the AMBROSIA project.

Publications & Manuscripts

Four publications or manuscripts constitute the membrane-related work of this PhD project. These are referred to by Roman numerals **I-IV**:

I Book chapter

Aschmoneit, F.J., Hélix-Nielsen, C. (2019) "Computational Fluid Dynamics Modeling of Forward Osmosis Processes", in *Current Trends and Future Developments on (Bio-) Membranes: Recent Advances on Reverse and Forward Osmosis*, pp. 85-111.

II Article

Aschmoneit, F.J., Hélix-Nielsen, C. (2020) "OMSD - An open membrane system design tool", in *Separation and Purification Technology, Vol 233*.

III Manuscript, finalized

Aschmoneit, F.J., Hélix-Nielsen, C. "Submerged-Helical Module Design for Pressure Retarded Osmosis"

The manuscript submission is withheld, due to an ongoing patenting process.

IV Manuscript outline

Aschmoneit, F.J., Hélix-Nielsen, C., "Fully Developed Mass Transfer and Pressure Drop in Spacer Filled Channels"

In addition, a not membrane-related study was conducted throughout this PhD project:

Article in print

Aschmoneit, F.J., Jensen, J.H., Saremi, S., Hélix-Nielsen, C. (2020) "Fluxes of sediment beneath floating silt screens due to density gradients and screen motion", in *Journal of Waterway, Port, Coastal, and Ocean Engineering*.

Contributions to Publications & Manuscripts

- I**
 - Definition of research objectives
 - Design and execution CFD simulations, collection and analysis of all data, interpretation of results
 - Writing the book chapter, creating the figures, revising the manuscript

- II**
 - Definition of research objectives, conducted literature review
 - Development of Simulink and Matlab code for simulation tool, collection and analysis of all data, interpretation of results
 - Writing the article, creating the figures, revising the manuscript

- III**
 - Definition of research objectives, conducted literature review
 - Development of CFD algorithm, development of computational mesh, execution of all simulations, collection and analysis of all data, interpretation of results
 - Writing the article, creating the figures

- IV**
 - Definition of research objectives
 - Development of CFD algorithm, development of computational mesh, execution of all simulations, collection and analysis of all data, interpretation of results
 - Creating the figures

Summary

Water stress affects an increasing part of the world population. In 2019, 2 billion people were estimated to live in water stressed countries, and around 30% of the world population doesn't have access to safe drinking water. Potable water production through water treatment is therefore essential for counteracting water stress and securing the supply of clean water. However, water treatment is energy intensive and exhibits a significant environmental impact. The energy-efficient treatment of water is therefore among our societies' most relevant challenges. Membrane technologies have become widely applied for the treatment of water, of which especially the desalination of seawater through reverse osmosis is substantial. Reverse osmosis applications are predominantly very energy intensive. Through the combination with energy-neutral forward osmosis or the energy-generating pressure retarded osmosis processes, the net energy consumption of reverse osmosis filtration processes can be lowered.

With regard to the high energy consumption of reverse osmosis filtration this PhD project is concerned with the efficiency optimization of reverse osmosis, forward osmosis, and pressure retarded osmosis processes. More specifically, the comprehensive objectives of this PhD project are the quantification and optimization of the above mentioned membrane separation processes through hydrodynamic modeling of flow- and solute transport mechanisms in the membrane-embedding module geometries. This thesis outlines and relates four studies which collectively depict the significance of the design of membrane modules.

The first part of this thesis focuses on the optimization of the reverse osmosis desalination process, whose process efficiency is governed by the total filtration rate, the filtrate purity, and the associated driving pressure. The most widely used module geometry for reverse osmosis is the spiral-wound module. It is assumed that its efficiency is most significantly affected by the feed channel and its embedded spacer. Through a computational fluid dynamics analysis of the spacer geometry, the effect of the spacer size and its orientation in the feed channel is quantified. It is found that thicker spacers marginally improve the water flux and decrease the pressure drop. In desalination applications with high salinity, the filtration efficiency is significantly increased when the spacers are not flow-aligned. Subsequently, the model of the spiral-wound module is applied in the development of a simulation tool for designing entire desalination plants, to which the same efficiency criteria apply. Through the simulation of different desalination designs, favorable application-specific con-

figurations are identified. All desalination designs are shown to be most efficiently operated at low feed flow rate and high feed pressure, disregarding membrane fouling.

The second part of this thesis focuses on osmosis-driven membrane processes, of which forward osmosis and pressure retarded osmosis are addressed. The efficiency of forward osmosis processes is governed by the permeation flux, the reverse salt flux, and the associated driving pressure. For the hollow fiber module the process efficiency is quantified against the packing density of the embedded fibers. Increasing the packing density yields a greater total membrane surface area, increases the cross flow, due to narrowing the channel, but also causes an increase of the driving pressure. An efficient trade-off between these effects is found for a packing density of $\sim 70\%$. In pressure retarded osmosis, the efficiency criteria are the power density, and the driving pressure. A novel, pressure retarded osmosis-specific module design is presented. The design uses submerged sheets of helically-twisted membranes to enforce the solute mixing in the draw channel. Due to its low packing density the design exhibits a very low pressure drop, and a low dilution level of the draw solution. The latter effect is compensated for by the recirculation of the draw solution. A computational fluid dynamics study shows that this pressure retarded osmosis -specific design is more effective compared to traditional filtration designs.

Dansk sammenfatning

Vandmangel påvirker i stigende grad verdens befolkning. I 2019 er det estimeret at 2 milliarder mennesker bor i lande påvirket af vandmangel, og omkring 30% af verdens befolkning ikke har adgang til rent drikkevand. Det er derfor essentielt at bekæmpe vandmangel og sikre forsyningen af rent drikkevand ved at udføre vandbehandling. Dog er vandbehandling energikrævende og har betydelig påvirkning på miljøet. Energi effektiv vandbehandling er derfor en af vores samfunds mest relevante udfordringer. Membranteknologier er blevet mere udbredt og anvendt i vandbehandling, her er afsaltning af havvand ved brug af omvendt osmose især vigtig. Omvendt osmose applikationer er hovedsageligt energi-intensive. I kombination med en energi-neutral fremadrettet osmoseproces, eller den energigenererende trykretarderede osmose proces, kan energiforbruget af omvendt osmosefiltrering sænkes.

Med hensyn til det høje energiforbrug ved omvendt osmose til vandfiltrering, har dette ph.d.-projekt fokuseret på effektivitetsoptimering af omvendt osmose-, fremadrettet osmose-, og trykretarderet osmose processerne. Specifikt er de omfattende mål i dette ph.d.-projekt, kvantificeringen og optimeringen af de ovennævnte membranseparationsprocesser gennem hydrodynamisk modellering af strømning og opløste stoffers transport-mekanisme i membranindlejrede modulgeometrier. Denne afhandling skitserer og relaterer de fire studier, der tilsammen tydeliggør signifikansen af membran-moduldesign.

Den første del af afhandlingen fokuserer på optimeringen af omvendt osmose afsaltningsprocessen, hvis effektivitet er styret af den totale filtreringsrate, filtreringsrenheden og det tilhørende driftstryk. Den mest anvendte modulgeometri for omvendt osmose er det spiral-viklede modul. Det antages, at dets effektivitet hovedsageligt er påvirket af feed-kanalen og den indlejrede spacer. Ved brug af computationel fluid dynamik analyse blev spacergeometrien, størrelsen og orienteringen i feed-kanalen kvantificeret. Det er fundet, at tykkere spacer forbedrer vandfluxen marginalt og sænker trykfaldet. I afsaltningsapplikationer med høj saltholdighed er filtreringseffektiviteten markant forbedret når spacerne ikke er strømningsflugtende. Efterfølgende blev modellen for det spiral-viklede modul anvendt i udviklingen af et simuleringsværktøj til design af hele afsaltningsanlæg, hvori de samme effektivitetskriterier gælder. Gennem simuleringen af forskellige afsaltningsdesign blev optimale applikationsspecifikke konfigurationer identificeret. Alle afsaltningsdesign viste at være mest drifteffektive ved lav strømningshastighed og højt feed-tryk, når der ses bort fra membranfouling.

Den anden del af denne afhandling fokuserer på osmose-drevne membranprocesser, her er fremadrettet osmose og trykretarderet osmose er undersøgt. Effektiviteten af fremadrettet osmoseprocessen er reguleret af permeationsfluxen, den modsatrettede saltflux og det tilknyttede driftstryk. For det hule fibermembran modul er proceseffektiviteten kvantificeret for pakningstætheden af de indlejrede fibre. Forøgelse af pakningstætheden giver et større totalt membranoverfladeareal og forøger tværflovet på grund af indskrækningen af kanalen, men forårsager også forhøjning af driftstrykket. Et effektivt kompromis mellem disse effekter er fundet for en pakningstæthed på $\sim 70\%$. I trykretarderet osmose er effektivitetskriterierne energitætheden og driftstrykket. Et nyt og originalt trykretarderet osmosespecifikt modul er præsenteret. Designet benytter neddykkede, spiralfordrevne membranark til at hæve opløsningsmiddelblandingen i draw-kanalen. På grund af dets lave pakketæthed udviser designet et meget lavt trykfald og en lav opløsningsgrad af draw-opløsningen. Den sidstnævnte effekt er kompenseret af recirkulationen af draw-opløsningen. Et computationelt fluid dynamik studie viser at, dette design er mere effektivt sammenlignet med traditionelle filtreringdesigns for trykretarderede osmose-applikationer.

Acknowledgements

First and foremost, I would like to thank my supervisor Claus Hélix-Nielsen. Claus has given me the freedom to formulate this project according to my ideas, within the supplied framework. From the start on, Claus showed trust in my independent development, which allowed me to spend time on gaining experience and shaping the project. Throughout the past four years, Claus has always been encouraging and supportive, which created a positive and productive working environment.

I also want to thank my collaborators in the *MEMENTO* and the *AMBROSIA* projects. Especially in the beginning of this PhD project, Peter Vittrup Christensen supported me through professional discussions and constructive criticism on the CFD modeling of membrane separation processes. Jörg Vogel and Brett Holmberg are thanked for guidance and sharing their membrane technology expertise with me. Yunfeng Li is thanked for his professional and inspiring project management in a difficult collaboration with a contractor.

My external stay at *DHI's* coastal engineering department in Kota Kinabalu, Malaysia, has been a very enriching experience, both professionally and culturally. I want to thank Jacob Hjelmager Jensen and Sina Saremi for offering me an interesting project and for sharing their expertise in CFD modeling. Also thanks to Kim Jacobsen and all my coworkers in Kota Kinabalu for making my stay so pleasant and rewarding.

DTU-Environment is fortunate to have its own IT support. Hugo Maxwell Connery is thanked for his support in adjusting Linux operating systems, and for fixing my convoluted Git repositories. Also DTU's central support group for the high performance computers contributed to this project. Especially Sebastian Borchert and Andrea Bordoni are thanked for their instant assistance with problems concerning the HPC.

I want to thank my former students Aske and Eleonora. Your projects also involved a steep learning curve for me: I learned so much from supervising you. It was a pleasure to be working with you, and I wish you all the best for your future.

DTU-Environment is an enormously welcoming and friendly place. Already soon after I started my PhD project, have many colleagues become friends. Thanks to Alex, Bas, Camilla, Carina, Carlos, Carson, Florian, Jan, Jane, Jonas, Klaus, Manfred, Marta, Pauly, Pedram, and Sigurd for making the past four years so special.

My non-DTU support group also contributed to this project: I want to thank Basti for Tuesdays with discussions ranging from the big bang to salt concentration gradients. Thank you, Lars, for your assistance and encouragement throughout so many years. Thanks to Line for your unconditional devotion and support. And, most importantly, thanks to my parents for all your help, inspiration and advice. Your commitment has always been immensely supportive!

Contents

| | |
|---|-----------|
| Preface | i |
| Summary | iii |
| Dansk sammenfatning | v |
| Acknowledgements | vii |
| Lists of Abbreviations & Symbols | xi |
| 1 Introduction | 1 |
| 2 Modeling of membrane separation processes | 7 |
| 2.1 Background on membrane separation processes | 7 |
| 2.2 Membrane flux equations for flat sheet membranes | 10 |
| 2.3 Governing flow and transport equations in fluid mechanics | 13 |
| 2.4 Computational fluid dynamics in membrane science | 15 |
| 3 Exhausting reverse osmosis performance | 19 |
| 3.1 Skew-oriented feed spacers in spiral-wound modules enhance reverse osmosis efficiency | 20 |
| 3.2 Upscaling reverse osmosis: Efficient designs for desalination plants | 29 |
| 4 Advancing osmosis-driven membrane technologies | 37 |
| 4.1 Optimized packing density of hollow fiber modules for forward osmosis | 38 |
| 4.2 Efficient green energy generation with pressure retarded osmosis | 45 |
| 5 Conclusions & Outlook | 53 |
| Bibliography | 56 |

Lists of Abbreviations & Symbols

| Abbreviation | Description |
|---------------------|-------------------------------------|
| AnMBR | Anaerobic membrane bioreactors |
| CFD | Computational fluid dynamics |
| ECMP | Electrochemical mambrane process |
| ECP | External concentration polarization |
| FO | Forward osmosis |
| HF | Hollow fiber |
| HFM | Hollow fiber module |
| ICP | Internal concentration polarization |
| MES | Membrane envelope sheet |
| ODMP | Osmosis driven membrane process |
| PAO | Pressure assisted osmosis |
| PDMP | Pressure driven membrane process |
| PL-FR | Plate-and-frame module |
| PRO | Pressure retarded osmosis |
| PS | Permeate-staging |
| PX | Pressure Exchanger |
| RED | Reverse electrodialysis |
| RO | Reverse osmosis |
| RS | Retentate-staging |
| SHM | Submerged-helical module |
| SP | Single-pass |
| SWM | Spiral-wound module |
| TFC | Thin film composite |
| TRB | Hydro turbine |

| Symbol | Description |
|---------------|---|
| A | Water permeability coefficient |
| B | Solute permeation coefficient |
| c | Solute concentration |
| d | Spacing of hollow fibers |
| D | Solute diffusion coefficient |
| d_h | Hydraulic diameter |
| f | Darcy friction factor |
| j_w | Water flux |
| j_s | Solute flux |
| k_d | Mass transfer coefficient |
| l_m | Length of membrane |
| p | Pressure |
| Q | Volumetric flow rate |
| $R_{0,1}$ | Inner/outer hollow fiber radius |
| Re | Reynolds number |
| S | Structural parameter |
| S_c | Solute source |
| Sh | Sherwood number |
| u | Velocity |
| α | Spacer orientation |
| β | Recirculation parameter |
| δ | Membrane support thickness |
| δp | Pressure drop |
| δQ | Permeation flow rate |
| Δp | Pressure difference across membrane |
| $\Delta \pi$ | Osmotic pressure difference across membrane |
| ϵ | Membrane support porosity |
| η | Dynamic viscosity |
| γ | Packing density |
| π | Osmotic pressure |
| Ψ | Dimensionless dummy variable |
| ρ | Density |
| τ | Membrane support tortuosity |
| ε | Twisting rate |
| ξ | Van 't Hoff coefficient |
| ζ | Bulk viscosity |

1 Introduction

The United Nations identified the need for *clean water and sanitation* and *affordable and clean energy* as two of the sustainable development goals (“Sustainable Development Goals,” 2015). According to their recent world water development report, over 2 billion people live in water stressed countries and around 4 billion people are affected by severe water scarcity for one month of the year or longer. Around 30% of the world population do not have access to safe drinking water, almost 50% of the world population drink water from unprotected surface water sources, and 60% of the world population do not have access to sanitation systems. Generally, the water stress level is expected to further increase. This development is driven by population growth, socio-economic development and changing consumption patterns. (“The United Nations World Water Development Report,” 2019). The growing need for fresh water causes severe problems: Ground water reservoirs are excessively used to meet the demand for fresh water leading to a depletion of the ground water level (Dalin, Wada, Kastner, and Puma, 2017). In parts of the world without ground water, potable water is often produced from desalinating sea water, or from the treatment of waste or surface waters at great energy expenses (Semiat, 2008), (“Significant Desalination Market Points,” 2013). In addition, the supply of energy has an environmental impact, also on surface- or ground waters, through the release, spillage or leakage of contaminated water, oil or gas from coal mining, fracking or oil drilling (Schwarzenbach, Egli, Hofstetter, von Gunten, and Wehrli, 2010), (Kačaroğlu, 1999). The production of clean water by energy-efficient means and the generation of energy by environmentally sustainable means are closely linked challenges and developing related solutions are among our society’s most crucial obligations.

Within the water-energy nexus membrane separation processes are widely applied filtration methods for the treatment of waste waters or seawater desalination. New membrane processes have the potential to cut the energy demand for filtration processes, or to generate green energy in an environmentally sustainable manner. Among various separation and purification processes for water treatment, membrane technologies have become matured and widely applied filtration methods. Most applications can be categorized as pressure driven membrane processes (*PDMP*), where hydraulic pressure drives a flow through the membrane, while particles or solutes are retained at the membrane. Another category of membrane applications are osmosis driven membrane processes (*ODMP*), where an osmotic potential gradient drives the flow across the membrane. Finally, electrochemical membrane processes (*ECMP*) are used in ion separation applications, i.e. in water filtration or energy generation ap-

plications. The most relevant membrane processes for the water-energy nexus are summarized as:

Reverse osmosis (RO) is a widely applied purification *PDMP*, e.g. for seawater desalination or water treatment. RO has matured throughout decades of research in membrane and module development. However, because the process is driven by a hydraulic pressure against an osmotic gradient, RO remains an energy-intensive and expensive-in-operation purification process.

Forward osmosis (FO) is an alternative *ODMP* for solute separation or water purification. Driven by an osmotic gradient, FO is potentially very energy-efficient, though, requiring a draw stream of high osmotic potential. Its commercial value is much debated and only few commercial products exist. FO is applied in combination with RO, or as a derivative processes, such as PRO or AnMBR.

Pressure retarded osmosis (PRO) is an energy generation *ODMP* which utilizes a salinity gradient across a membrane to create a pressurized flow, which in turn drives a hydro turbine. Except from a few individual cases, this process is not commercialized. Various challenges will have to be met, in order to have PRO technologies to competitive energy generation systems.

Osmotic anaerobic membrane bioreactors (AnMBR) is a combined energy generation and wastewater treatment *ODMP*, in which a wastewater stream is upconcentrated through FO, while anaerobic digestion in the organic wastewater produces methane. The AnMBR hybrid process has great potential, but the technology will need to mature before its commercial application.

Reverse electro-dialysis (RED) is an energy generation *ECMP*, through which an ion current is generated by electro-osmotic potentials between stacked reservoirs of alternating salinity, separated by ion exchange membranes. RED is potentially the most efficient process for generating energy from mixing salt- and fresh water, but at its current development stage, the energy generation rate is not competitive.

There is a growing interest in *ODMPs* and *ECMPs* for water treatment and energy generation, due to their higher eco-efficiency potential, while *PDMPs*, mostly, still exhibit a higher cost-efficiency. Despite the different maturity level of the above mentioned membrane processes, their respective ongoing technology development can be categorized alike, into:

Membrane development, i.e. maximizing water flux, or ion exchange rates, and mechanical strength, while minimizing solute leaking and fouling/scaling propensity.

Module design, i.e. maximizing the solute separation-, water purification-, or energy generation rate, while minimizing operation costs and fouling/scaling propensity.

Process benchmarking, i.e. the quantification of a process efficiency, when exposed to specific applications and conditions.

System optimization, i.e. maximizing the solute separation, water purification, or energy generation rate, while minimizing operation costs, and the optimization of hybrid processes, including combinations of membrane technologies.

The optimization of the earlier mentioned membrane processes by means of the above mentioned development branches was organized through two projects within which this PhD project was incorporated:

The MEMENTO (Membrane Energy Technology Operations) project aims at enhancing *ODMP* and *ECMP* efficiencies to an industrially competitive scale, with a main focus on three key-processes: AnMBR, PRO and RED, (“MEMENTO,” 2019). More specifically, the project aims are defined as: (i) membrane development of biomimetic FO and PRO membranes, (ii) membrane development of ion exchange membranes for the application in RED, (iii) module optimization for FO, PRO and RED processes through computational fluid dynamics (CFD) analyses, and (iv) process benchmarking of an AnMBR operated with industrial effluents. The advancement of these three processes is coordinated between the MEMENTO project collaborators taking advantage of each collaborators’ area of expertise: At the *Technical University of Denmark* the three key processes’ efficiencies are quantified through experimental test bench setups and computational fluid dynamics models. The *University of Copenhagen* contributes with expertise in protein production for biomimetic membranes and their functional characterization. They also provide the supply of selected ion channels used for ion exchange membranes. *Aquaporin A/S* provides the biomimetic osmotic membranes. *Grundfos A/S* provides testing facilities for FO and PRO, as well as techniques for membrane fouling analysis. *DHI* contributes with feasibility and cost-effectiveness analyses of AnMBR in different applications. The *Colorado School of Mines* (USA) investigates the applicability of PRO with wastewater streams. The *University of Maribor* (Slovenia) contributes

with their knowledge on membrane surface characterization and membrane fouling quantification.

The AMBROSIA (Aquaporin-Inside Membranes for Brackish Water Reverse Osmosis Applications) project aims at enhancing reverse osmosis efficiencies for brackish water applications, through the development of RO membranes with Aquaporin's biomimetic water channels. The project aims at (i) developing optimized flat sheet membranes for the application in brackish water RO, (ii) the development of a CFD model for the optimization of the membrane-embedding module, and (iii) the process benchmarking with designed membranes and modules in different industrial scenarios.

Research objectives

This PhD study contributes to the above mentioned projects through theoretical studies on module design and system optimization, for the RO, FO, and PRO. More specifically, given the prospect and challenges of these three membrane processes, this PhD project's objectives are defined as:

- O1** The quantification and optimization of the effect of spacer thickness and orientation in spiral-wound modules on the filtration rate and pressure drop, for RO desalination applications.
- O2** The quantification and optimization of the effect of the packing density in hollow fiber modules on the separation rate and pressure drop, for FO applications.
- O3** The design and performance quantification of a PRO-specific module geometry.
- O4** The development of a filtration plant simulation tool and its applications in finding efficient plant designs and corresponding operating conditions.

Referring back to the Sustainable Development Goals, this project contributes to goals six and seven, through the development of technologies that increase water-use efficiency through recycling, desalination, wastewater treatment and renewable energy generation.

Thesis structure

This thesis follows the development stage of the three membrane processes of interest, from miniature design alteration for the well-matured RO technology, over geometry optimizations of a module type for the emerging FO technology, to novel, fundamental design suggestions for PRO applications.

Chapter 2 gives a background on membrane processes, theoretical models for the description of membrane water flux and solute leaking, and how CFD is applied for membrane module performance analyses.

Chapter 3 is concerned with the optimization of RO through two studies: A model for the RO filtration performance is developed, based on the hydrodynamics in the feed channel. Subsequently, a simulation tool for efficiency analyses of industrial-scale desalination plants is presented and its application demonstrated in two desalination case studies.

Chapter 4 is concerned with the optimization of ODMPs through two studies: The first study analyses how the packing density in hollow fibers modules affects the FO osmotic permeation rate and the consequent pressure drop along the module. The second study introduces a novel, PRO-specific module design, whose efficiency is quantified through a study on its geometry and optimal operation conditions.

Chapter 5 summarizes the study outcomes and aligns them with the before-stated research objectives.

2 Modeling of membrane separation processes

'All models are wrong' (Box, 1976). However, through careful considerations of the underlying physics they allow to distinguish between significant and insignificant dependencies of physical processes. A model can be regarded as a set of assumptions reducing a physical process to its fundamental principles. Thereby, models adhere to the virtue-of-simplicity dogma: The more simplistic the model, the greater its potential expressiveness. This chapter introduces models for water- and solute transport through membranes and how the flow in membrane modules is approximated through CFD models.

2.1 Background on membrane separation processes

Semi-permeable membranes separate water or gas reservoirs of different solute concentration and hydraulic pressure. Discontinuities of solute concentration across the membrane cause an osmotic potential across the membrane. Figure 2.1 shows a sketch of a fresh water reservoir (left) and a saline water reservoir (right). The saline reservoir has a higher osmotic potential, due to its greater solute (salt) concentration. This potential difference is equilibrated by the permeation of water from the fresh water side, through the membrane, to the saline reservoir. This process is known as osmosis or forward osmosis. Osmosis can be counter-acted or reversed by a hydraulic pressure difference across the membrane. For a given osmotic potential difference across the membrane, there exists a hydraulic pressure difference $\Delta p'$ which counter-acts and halts osmotic water permeation. In membrane science and throughout this study the osmotic potential is referred to as the osmotic pressure π . The osmotic pressure difference $\Delta\pi$ is a pseudo pressure which is equal to the equilibrium hydraulic pressure difference $\Delta p'$. As indicated the osmotic pressure depends on the solute concentration c :

$$\pi = f(c) \tag{2.1}$$

The water flux through the membrane j_w is governed by the osmotic pressure difference $\Delta\pi$ and the supporting, or counter-acting hydraulic pressure difference Δp :

$$j_w = f(\Delta\pi, \Delta p) \tag{2.2}$$

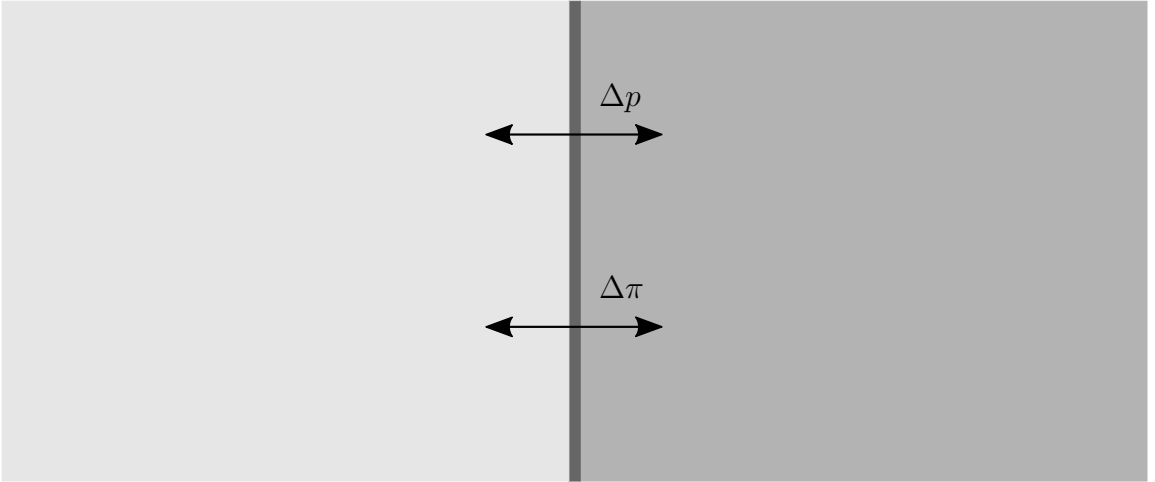


Figure 2.1: The magnitude and direction of the water permeating the membrane depends on the magnitude and sign of Δp , compared to the osmotic pressure difference $\Delta\pi$.

The different membrane processes are defined through the relation of $\Delta\pi$ and Δp : FO describes the case of $\Delta p = 0$. If $\Delta p < 0$ the hydraulic pressure supports osmotic water permeation which is called pressure assisted osmosis (PAO). In the case of $0 < \Delta p < \Delta\pi$ the hydraulic pressure difference counter-acts, but doesn't reverse osmosis. This is known as PRO. Finally, $\Delta\pi < \Delta p$ refers to RO, where the hydraulic pressure difference counter-acts and reverses the osmotic water permeation. The three processes PAO, FO and PRO are collectively referred to as ODMP, for which the water permeates from a feed reservoir into a higher-concentrated draw reservoir. RO, and its functionally related processes micro filtration, ultra filtration and nano filtration, are referred to as PDMP¹. In PDMP the water permeates from a concentrated feed reservoir into a permeate reservoir. Figure 2.2 summarizes how the relation of $\Delta\pi$ and Δp define the different membrane processes.

The water permeation through a membrane does not only depend on the osmotic- and hydraulic pressure difference, but also on the membrane characteristics. This study only considers the commonly applied Thin Film Composite (TFC) membranes. These consist of a thin ($\mathcal{O}(10^{-7}m)$) active separation layer and a support structure ($\mathcal{O}(10^{-4}m)$) providing mechanical stability. The water permeation rate through a TFC membrane is predominantly governed by its water permeability coefficient A , $[A] = l m^{-2} h^{-1} bar^{-1}$. An ideal semi-permeable membrane retains all solute,

¹The related processes concern the filtration of particles and compounds of nm scale or greater. These filtration processes are fundamentally similar to RO and are not considered in this study.

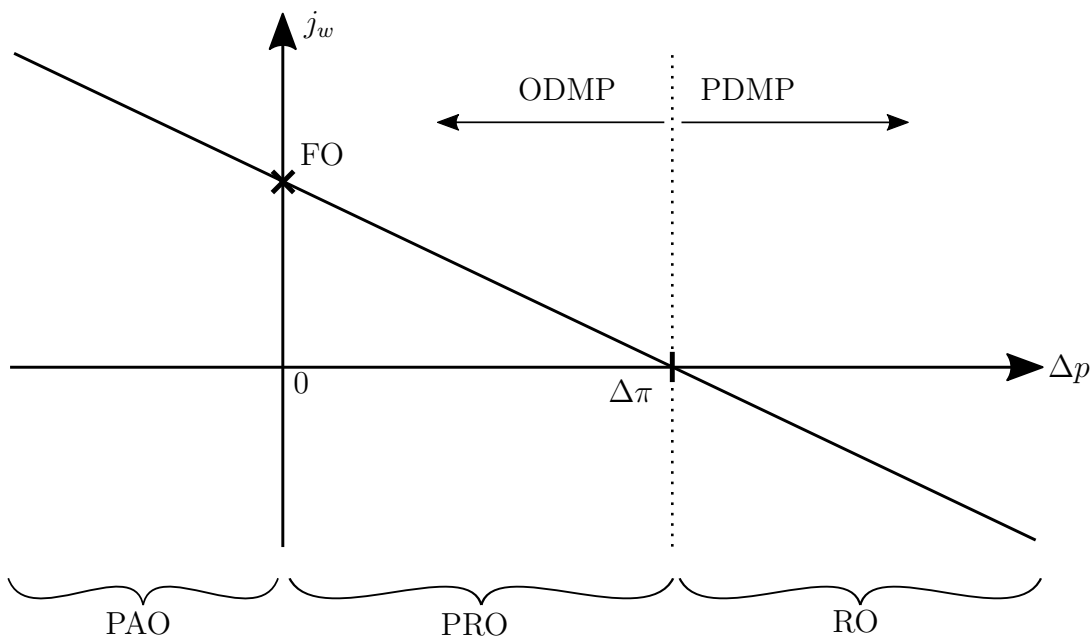


Figure 2.2: Membrane processes are distinguished by the relation of $\Delta\pi$ to Δp . Under the assumption $J_w \sim \Delta\pi - \Delta p$, and a fixed $\Delta\pi$, the graph shows how the hydraulic pressure difference defines the membrane process.

while water can permeate through it. Real membranes, however, always leak solute which leads to an absolute solute transport across the membrane. The membranes' leaking characteristic is quantified through the solute permeation coefficients B , $[B] = kg\ m^{-2}h^{-1}$, describing the leaking rate for a given solute. Throughout this study only *NaCl* solutions are considered and all listed solute permeation coefficients refer to this salt. The salt leaking affects the effective osmotic pressure difference and therefore also the water flux. The support layer of the membrane also affects the water flux as its porous structure poses a flow resistance which has the retention or accumulation of solute within the support layer as a consequence, affecting the effective osmotic pressure difference. This effect is known as internal concentration polarization (ICP) which is governed by the solute leakage and the support layer characteristics. It is quantified through the structural parameter $S = \delta\tau/\epsilon$, $[S] = m$ which is defined by the layer thickness δ , its porosity ϵ , and tortuosity τ . The water flux through the membrane therefore depends on the membranes' intrinsic characteristics:

$$j_w = f(A, B, S) \quad (2.3)$$

For a given membrane process the membranes are embedded in application-specific membrane modules. The membrane modules are a crucial factor for the efficient

application of membrane processes. They govern the hydrodynamics around the membranes and therefore affect the local solute concentration and pressure. They also define for which operating conditions, in terms of cross flow and applied pressure, the membrane process works efficiently. Finally, the process operation costs are often significantly linked to generating the driving pressure, necessary to overcome the modules' flow resistance. The module design governs the processes' pressure drop. The membrane process efficiency is therefore closely related to the module geometry and its operation:

$$j_w = f(\text{module geometry, process operation}) \quad (2.4)$$

$$\delta p = f(\text{module geometry, process operation}) \quad (2.5)$$

The following chapter 2.2 describes which assumptions on equations (2.2) and (2.3) define the water permeation for different membrane processes. The quantification of how module designs and their operation affects the process efficiency is a fundamental part of this thesis and will be investigated in chapters 3.1, 4.1 and 4.2, for RO, FO and PRO, respectively.

2.2 Membrane flux equations for flat sheet membranes

The membrane flux equations define dependencies in equations (2.2) and (2.3), based on the membrane process, and its orientation. Figure 2.3 shows the membrane cross section, together with the associated solute concentration profile across the membrane, for (a) RO, (b) FO, and (c) PRO. The three sketches show cross sections of flat sheet TFC membranes, which are composed of a thin active layer and a thick porous support layer. For all membrane processes, the water and solute fluxes are directly dependent on the effective concentration difference across the active layer. As can be seen in the three sketches, the effective concentration difference is affected by concentration gradients within and around the membrane: As water permeates through the membrane, while the solute is mostly retained, solute accumulates in the membrane vicinity on the feed side. On the permeate side (RO) or draw side (FO,PRO) the water flux causes a local dilution of the solute. These two effects are known as concentrative- and dilutive external concentration polarization (ECP). They affect the osmotic pressure on either side of the membrane and therefore increase (RO) or reduce (FO,PRO) the effective osmotic pressure difference, reducing the water flux in either case. Furthermore, concentration within the membrane, internal concentration polarization (ICP), further reduces the effective osmotic pressure difference, and thereby reduces the membrane flux further (FO,PRO).

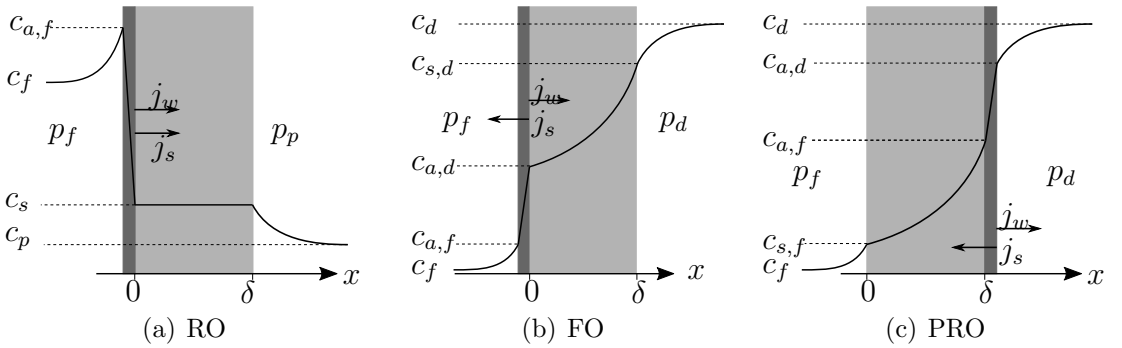


Figure 2.3: Conceptual sketches illustrating concentration profiles in membrane cross sections.

In this section, the equations for the water flux j_w and the solute flux j_s are derived for the different membrane processes. These fluxes act as boundary conditions for the subsequent computational fluid dynamics models.

An underlying assumption for all processes is the validity of the van 't Hoff equation which defines a direct proportionality between the osmotic pressure and the solute concentration. This equation defines equation (2.1) as:

$$\pi = \xi c, \quad (2.6)$$

where ξ is the proportionality constant. The validity of the van 't Hoff equation depends on the solute. For saline solutions it is assumed accurate for concentrations of up to 1.5 M.

RO water and solute flux equations

In RO, the water flux is directed against the concentration gradient, i.e. from the feed side towards the permeate side. Therefore, the solute flux is also directed towards the permeate reservoir, see Fig. 2.3(a). In order to minimize ICP effects, the membranes are typically oriented with the active layer facing the feed stream (AL-FS). Figure 2.3(a) shows the concentration profile across the membrane in RO operation: The feed bulk concentration c_f gets upconcentrated in the membrane vicinity, due to the water permeation and solute retention, i.e. concentrative ECP, which increases the local solute concentration to $c_{a,f}$ at the membrane surface. The water flux across the flat sheet membrane is governed by the water flux across the active layer, across which the osmotic separation takes place. In the case of RO, the dependencies in equations (2.2) and (2.3) are simply modeled as:

$$j_w = A(p_f - p_p - \pi_{a,f} + \pi_s) \quad (2.7)$$

Similarly, the solute flux is proportional to the effective concentration difference across the membrane:

$$j_s = B(c_{a,f} - c_s) \quad (2.8)$$

Because of the aligned fluxes of water and solute, and because of the AL-FS membrane orientation, concentration gradients within the support layer are assumed to be insignificant, and thus, ICP can be neglected in the flux equations.

FO water and solute flux equations

In FO the water permeation is driven by the osmotic gradient only, i.e. $\Delta p = 0$. The water flux direction is therefore aligned with the concentration gradient across the membrane, in contrast to RO. This has the consequence, that the water and solute fluxes are opposing each other, causing a concentration gradient within the support structure, i.e. ICP. Figure 2.3(b) shows the concentration profile of a TFC membrane in FO application. The water- and reverse salt fluxes are governed by the effective concentration difference across the active layer:

$$j_w = A(\pi_{a,d} - \pi_{a,f}) \quad (2.9)$$

$$j_s = B(c_{a,d} - c_{a,f}) \quad (2.10)$$

Because the characteristic length scale of the support structure is much smaller, $\mathcal{O}(10^{-4}m)$, than the length scale of the membrane module, $\mathcal{O}(1m)$, it is not feasible, to resolve the support in the CFD model. Alternatively, the solute profile within the support can be calculated from integrating the convection-diffusion equation (2.21) between the active layer and the draw channel. For flat sheet membranes the flux of water and solute through the support can be assumed constant. The water flux equation across the active layer and the support can be solved to (Loeb, Titelman, Korngold, and Freiman, 1997):

$$j_w = \frac{D}{S} \ln \left(\frac{A\pi_{s,d} + B}{A\pi_{a,f} + B + j_w} \right) \quad (2.11)$$

The resulting water flux equation (2.11) is no longer depending on the unknown concentration $c_{a,f}$, but is transcendental and must be solved numerically instead.

The solute flux equation (2.11) can be expressed through the water flux through:

$$j_s = \frac{B}{A\xi} j_w \quad (2.12)$$

PRO water and solute flux equations

As PRO is an ODMF the fluxes of water and solute are opposing each other which causes significant ICP. The concentration profile through the membrane is sketched in Fig. 2.3(c). In PRO the membranes are usually oriented with the active layer facing the draw side, as opposed to FO. Across the active layer the water and salt fluxes are defined as:

$$j_w = A(\pi_{a,d} - \pi_{a,f} - p_d + p_f) \quad (2.13)$$

$$j_s = B(c_{a,d} - c_{a,f}) \quad (2.14)$$

The effect of ICP can be incorporated in the flux equations by solving the convection-diffusion equation (2.21) within the membrane support layer (Lee, Baker, and Lonsdale, 1981), yielding:

$$j_w = A \left\{ \frac{\pi_{a,d} - \pi_{s,f} \exp\left(\frac{j_w S}{D}\right)}{1 + \frac{B}{j_w} \left[\exp\left(\frac{j_w S}{D}\right) - 1\right]} - \Delta p \right\} \quad (2.15)$$

The solute flux (2.14) is expressed by the water flux through:

$$j_s = \frac{B}{\xi} \left(\frac{j_w}{A} - \Delta p \right) \quad (2.16)$$

2.3 Governing flow and transport equations in fluid mechanics

The hydrodynamic variables of interest in this thesis are the local flow field, expressed through the velocity vector u_i , the pressure p , and a scalar quantity φ , which represents the local solute concentration or osmotic pressure. These variables are governed by the conservation laws of mass, momentum, and the scalar quantity. Throughout all the following studies only water or saline water solution are considered. Water can be considered as incompressible, i.e. its density doesn't change when pressurized, and Newtonian, i.e. its internal shear forces are proportional to the velocity gradient. These two characteristics will allow to significantly simplify the governing equations.

The equation of mass conservation states that for a control volume dV with density ρ , the rate of mass change is given by the divergence of the mass flux through that volume:

$$\partial_t \rho = -\partial_j (u_j \rho), \quad (2.17)$$

Since water can be assumed as incompressible, and the solute concentration is assumed to only have a negligible effect on the water density, the density can be assumed constant. That reduces equation (2.17) to the *Continuity Equation*:

$$\partial_j u_j = 0. \quad (2.18)$$

Incompressible flow is thus divergence-free.

The governing equation of momentum conservation are the *Navier-Stokes Equations*, which are the fluid system equivalent to *Newton's Second Law* (A particle's change of momentum is given by the total force acting on it). The rate of change of fluid momentum per dV is affected by bulk fluid motion, pressure differences, internal friction or compression, and external forces, such as gravity. In its most general form the *Navier-Stokes Equations* are written as (Landau and Lifshitz, 1987):

$$\partial_t(\rho u_i) + u_j \partial_j(\rho u_i) = -\partial_i p + \partial_j \left[\eta \left(\partial_j u_i + \partial_i u_j - \frac{2}{3} \delta_{ij} \partial_k u_k \right) \right] + \partial_i (\zeta \partial_j u_j) + \rho f_i, \quad (2.19)$$

where η is the dynamic viscosity, ζ is the bulk viscosity, and f is an external force.

Under the assumptions of incompressibility and Newtonian shear forces, this equation can be simplified significantly:

$$\rho \partial_t u_i + \rho u_j \partial_j u_i = -\partial_i p + \eta \partial_{jj} u_i + \rho f_i \quad (2.20)$$

However, the resulting equation is a 2nd order partial differential equation, for which no closed form is known. It therefore has to be solved numerically.

The *Convection-Diffusion Equation* is similar to the mass conservation equation, but also allows for the diffusive solute transport and a scalar source S_c :

$$\partial_t c + \partial_j (u_j c) - \partial_j (D \partial_j c) = S_c, \quad (2.21)$$

Another important equation for the subsequent solution algorithm for the incompressible *Navier-Stokes Equations* (2.20) is the *Pressure-Poisson Equation*. Incompressible flow was shown to be divergence-free. Applying the divergence operator to equation (2.20) yields:

$$\partial_{kk} p = \partial_k (u_j \partial_j u_k + \rho f_k) \quad (2.22)$$

2.4 Computational fluid dynamics in membrane science

CFD is a collective term for a series of mathematical operations allowing to approximate solutions to fluid problems, which are governed by partial differential equations. In the presented CFD studies the governing flow equations are (2.18), (2.20), and (2.21). Throughout this PhD project, CFD is the key-tool for assessing how the membrane module design affects the efficiency of the separation processes. All CFD simulations are conducted with the free and open source software tool *OpenFOAM* (OF) (The OpenFOAM Foundation, 2018). OF's major advantage over alternative, commercial CFD tools is its open development, which allows for the modification or extension of the tool with custom solvers or post-processing functions. However, the imperfect documentation and customer support cause a steep learning curve and in some cases also lengthy work progress. The projects **I**, **III**, and **IV** are based on OF simulations. For each of these projects, an example case and potential key-modifications are published in the respective referenced repositories. This chapter presents a condensed description of the fundamental processes, which collectively prepare a CFD study for its subsequent application in fluid dynamic simulations. References are given for more in-depth information of the respective processes.

Definition of particular model

The particular model is the set of all assumptions, from which the governing fluid dynamics equations and boundary conditions are derived. All assumptions must be rooted in a profound understanding of the governing physics. The distinction between significant and insignificant dependencies must relate to the model's purpose.

Throughout the presented studies in this thesis, the assumptions on the fluid systems are similar. Chapter 2.3 states the underlying assumptions and how they define the simplified governing flow and transport equations. In all CFD studies, the membranes are modeled as boundary conditions, which locally define the water- and solute flux, based on the membrane characteristics and the ambient hydrodynamics. The derivations of the membrane boundary conditions from their governing assumptions are outlined in Chpt. 2.2.

Discretization of computational domain

The computational domain refers to the fluid-filled space and its bounding surfaces, which are usually defined by computer aided design (CAD) programs. For solving the discretized governing equations in the fluid domain, the computational domain needs to be discretized in small volumetric elements, which collectively form the

computational mesh. The design of the computational mesh is a crucial part of a CFD study, as the stability and accuracy of the CFD algorithm decisively depends on the mesh type and its quality. The mesh resolution affects the computation time and model accuracy, since no flow patterns can be resolved, that are smaller than the mesh spacing. Therefore, the applied mesh resolution poses a compromise between accuracy and computation time.

All computational meshes in the presented CFD studies are generated with OF's `blockMesh` utility, which produces hexahedral meshes based on scripts, defining the geometries and their decomposition. Since these scripts are extensive text files, they are not included in this thesis. However, these *blockMeshDicts* can be found in the supplied example case repositories.

Selecting solution algorithm

Based on the particular model, the solution algorithm, or 'solver', is selected. Various solvers are specialized with respect to specific fluid systems. These specify the algorithms, which solve the governing equations and their boundary conditions.

As described in Chpt. 2.3, all fluid systems in this study are considered incompressible and Newtonian. Furthermore, only steady state solutions to the membrane separation processes are of interest. For this combination of prerequisites, the SIMPLE (Semi Implicit Method for Pressure Linked Equations) (Patankar, 1980) algorithm defines the solution sequence, through which the fluid system is solved. It iteratively predicts solutions to the momentum equations, i.e. the *Navier-Stokes Equations*, which are subsequently corrected through the *Pressure-Poisson Equation*.

Discretization and linearization of governing equations

This procedure transforms the continuous governing flow equations, which are defined by the particular model and the solution algorithm, into discrete equations, according to specified discretization schemes for all spacial- and temporal derivatives. For every fluid variable x the discretized governing equations are rearranged into linear algebraic equations of the form:

$$A_{i,j}x_i = b_j, \tag{2.23}$$

with the coefficient matrix $A_{i,j}$ and the source term b_j . The dimensions of A , x , and b relate to the size of the computational mesh N as: $A \in \mathbb{R}^{N \times N}$, $x \in \mathbb{R}^N$, and $b \in \mathbb{R}^N$. The choice of the discretization scheme affects the stability, accuracy, and computation time of the CFD algorithm. Detailed information on the discretization and linearization are found in (Moukalled, Mangani, and Darwish, 2016).

The discretization and linearization is automated through OF. Nevertheless, the specific discretization schemes for all derivatives must be specified. As all CFD studies include steady-state simulations only, discretization schemes for temporal derivatives are not specified. OF allows for the specification of gradient, divergence, and laplacian discretization schemes, for every flow variable individually. A complete description of all discretization schemes and their effects is very extensive and therefore omitted in this thesis. Generally, second-order-accurate schemes are employed, where stability and computation time allow that. However, the employed discretization schemes can be found in the *fvSchemes* file in the respective repository.

Solving linear equation system

The sets of linear algebraic equations (2.23) are solved for the fluid variables x through analytic or numeric methods. Because the spacial discretization schemes define the derivations of the flow variables based on few, neighboring flow variables, the resultant coefficient matrix A is sparse, i.e. only the entries in the vicinity of the diagonal are non-zero. Sparse linear systems are significantly faster solved by numerical algorithms, such as the projection method. The choice of the solver affects the stability and computation time of the CFD algorithm. Various linear equation solvers are described in (Meister, 2015).

OF offers a wide range of linear equation system solvers, which can be selected separately for every fluid variable. The *fvSolution* file in the respective example cases lists the employed solver for every variable's linear equation system.

Mesh accuracy analysis

Through the mesh accuracy analysis, the inherent discretization error is quantified. The discretization error converges asymptotically, as the resolution of the computational mesh is increased. A widely applied method for the mesh accuracy analysis is the *Grid Convergence Index* (GCI). It quantifies the relative difference of a simulated quantity and its converged value through a series of similar simulations, based on various mesh resolutions. The GCI test is conducted on the flow variable, which is most sensitive with respect to the mesh resolution. The quantification of the discretization error is of great importance, since it supports the trustworthiness of CFD analyses, and allows to chose a reasonable, but not unnecessarily high mesh resolution for subsequent simulations.

GCI analyses are conducted on all presented CFD studies. However, since these do not contribute to the comprehensive statements, they are omitted in this thesis, but are found in the respective publications.

3 Exhausting reverse osmosis performance

Potable water production with RO is extensively used in regions with limited ground water. In 2012 the primary sources of feed streams are seawater ($\sim 56\%$) and brackish water ($\sim 24\%$), with a global production rate of $78.4M m^3/d$. RO is very energy intensive, due to the high hydraulic pressure needed to overcome the osmotic pressure gradient. In a desalination plant approximately 44% of the total costs are apportioned to the electrical energy driving the pumps (“Significant Desalination Market Points,” 2013). RO is a well-advanced and matured technology. Nevertheless, because of its intensive use and its costly operation, merest efficiency improvements have a significant impact.

The efficiency of a RO process can be reduced to maximizing the filtration rate, while minimizing the associated operation costs, i.e. the pressure drop, and the solute leaking rate. Figure 3.1 shows a sketch of a RO module with its in-going and out-going water streams. The operating conditions are defined in the feed stream variables (Q_f, p_f, π_f) . Based on the module characteristics and the operating conditions, the process efficiency is evaluated from the variables $(\delta Q, \delta p, \pi_d)$. This generalization of the process efficiency holds for individual filtration modules and for entire desalination plants.

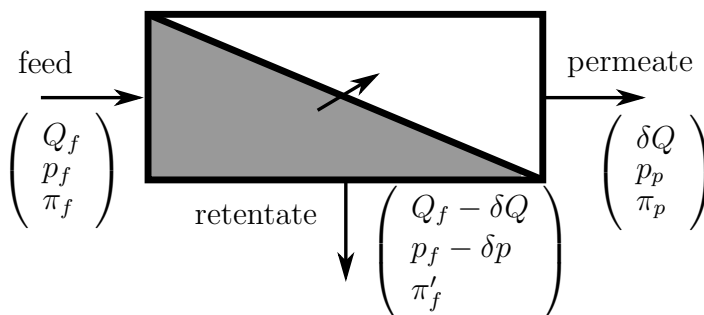


Figure 3.1: Schematic of a RO process with feed inflow, permeation stream, and retentate stream. Efficient RO modules exhibit a maximum filtration rate δQ , for a minimal pressure drop δp and permeate solute concentration π_p .

This chapter summarizes two studies concerning RO performance optimization: In the first part, the primarily applied SWM module is represented through a computa-

tional model, in which the effect of the feed spacer geometry variations are analyzed. In the second part, the efficiency of an industrial-scale desalination plant is simulated by considering various configurations and interconnections of several SWMs.

3.1 Skew-oriented feed spacers in spiral-wound modules enhance reverse osmosis efficiency

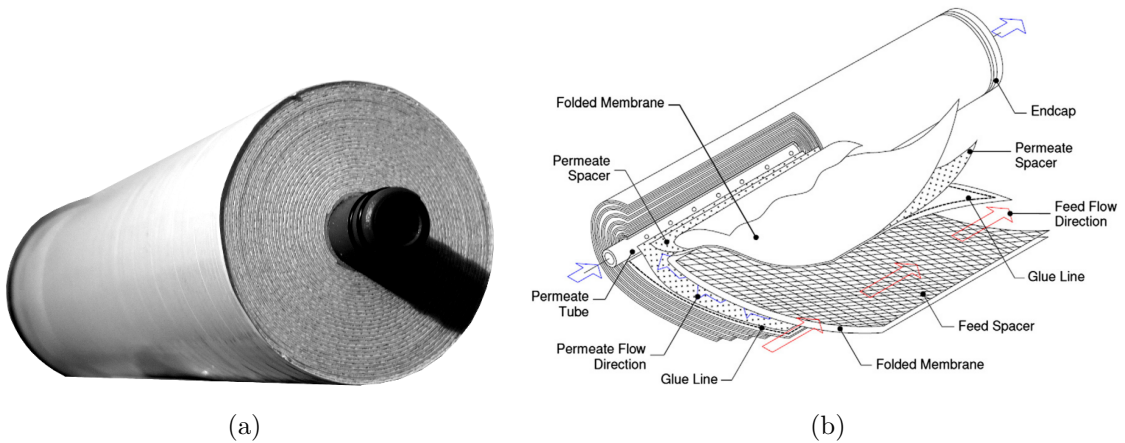


Figure 3.2: (a) Photo of a SWM indicating the high packing density through rolled up membranes and spacers. (b) Schematic illustration of the SWM indicating the feed flow with red arrows and the permeate channel with blue arrows. Adapted from (Karabelas, Kostoglu, and Koustou, 2015)

The SWM design is the predominantly applied module type for RO applications. Figure 3.2 presents a picture of an SWM on the left, and a schematic illustration on the right. Its particular design feature is the rolling of membranes and spacers around a central permeate tube, which allows an enormously high packing density of the membrane. More specifically, rectangular membrane double layers are separated by permeate spacers, and glued together along three of their edges. These are called membrane envelopes. Their open, fourth edge is connected to the central permeate tube. A number of these membrane envelopes are alternately rolled with feed spacers around the center permeation pipe. The pressurized feed stream enters the module through the rolled up, spiral-formed feed channel opening between the membrane envelopes, and pursues along the longitudinal direction, i.e. parallel to the center pipe orientation, through the SWM. A part of the feed stream permeates through the membrane inside the membrane envelope, from where the permeate flows through the wound-up permeate channel towards the center pipe, where the

permeate stream is collected and transported through the pipe.

The RO filtration performance is defined through the permeate solute concentration c_p , the filtration rate δQ , and the pressure drop along the module δp . The solute concentration is solely governed by the membrane characteristics, the filtration rate is governed by both, membrane characteristics and module design, and the pressure drop is governed by the module design alone. This study analyzes how the filtration rate and pressure drop are affected by the module design for a given set of membrane characteristics. It is hypothesized that the feed channel and its embedded spacer is the most significant design feature in an SWM. The feed spacers serve a double purpose: (1) They separate membrane sheets in the tightly rolled module, creating void space for the feed channel. (2) They disturb the cross flow and effectively mix the feed stream, which reduces concentrative ECP. The geometry of feed spacers affects therefore affects the filtration rate, but also the pressure drop across the feed channel.

The effect of the spacer geometry has been investigated in various studies. An early study (Schock, 1987) quantifies the mass transfer and pressure drop of several commercial spacers. The derived scaling relations allow for the prediction of optimal spacers for given RO applications. But the spacer thickness and its orientation are not taken into account. In (Lau, Abu Bakar, Ahmad, and Murugesan, 2009), the effects of different spacer orientations and strand angles are analyzed. Instead of the local mass transfer, they only consider the local shear stress on the membrane. It is concluded that not flow-aligned spacer orientations perform best with respect to the filtration rate and the pressure drop, but the simulation results are not quantified in terms of scaling relations. In a more recent study (Gu, Adjiman, and Xu, 2017), a comprehensive analysis was conducted on different spacer orientations, strand angles, and woven spacers. They conclude that the pressure drop is very sensitive with respect to the spacer orientation, that non-orthogonal spacers yield a lower water flux, and that woven spacers increase water flux but also the pressure drop. However, the results are not analysed in terms of scaling relations, and therefore, these general conclusions cannot directly be applied to different RO applications.

In the following, it is quantified how the spacer size and its orientation affect its solute mixing characteristics and its associated pressure drop. Through the derived scaling relations, a simple model the SWM filtration rate is defined. This model is subsequently used to evaluate the efficiency of different spacer orientations and thicknesses for desalination applications of brackish water, seawater, and brines. This chapter is based on **IV**.

The feed spacer is a periodic mesh of symmetric unit cells. Therefore, in this CFD study, the spacer characteristics are reduced to the characteristics of one unit cell.

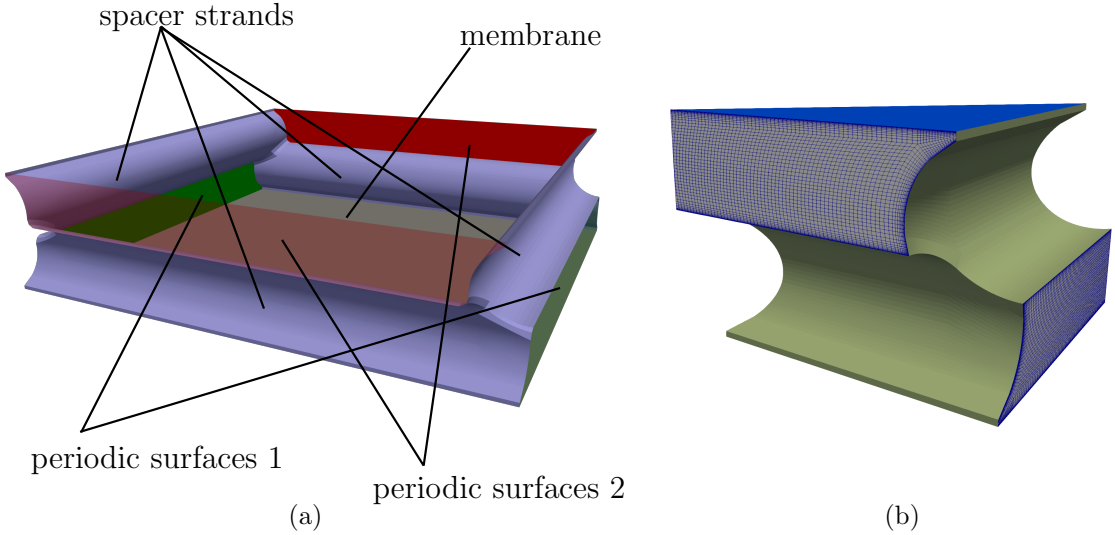


Figure 3.3: (a) The computational domain of a unit cell of an orthogonal spacer. (b) The computational mesh before mirroring indicating an increased resolution towards the boundaries to capture friction losses and steep solute gradients.

Figure 3.3(a) illustrates the computational domain of one orthogonal unit cell with dissected spacer strands separating the top and bottom membranes, and the two pairs of periodic surfaces. Two widely applied, commercial spacers are modeled in this study. The 28 mil spacer is applied for high filtration flow rates, while the thicker 34 mil spacer is used for challenging water, possibly causing membrane fouling. Their geometry parameters are summarized in Table 3.1.

Table 3.1: Geometry specifications for the two considered spacers: w is the width of the unit cell, h is the spacer height, d_h its hydraulic diameter, and ϵ its porosity.

| id | $d[mm]$ | $h[mm]$ | $d_h[mm]$ | ϵ |
|--------|---------|---------|-----------|------------|
| $d28m$ | 2.822 | 0.711 | 0.91 | 0.9 |
| $d34m$ | 3.629 | 0.867 | 1.14 | 0.9 |

The geometry was meshed in OpenFOAM's blockMesh utility. Fig. 3.3(b) shows the reduced mesh with an increasing resolution towards the spacer and membrane surfaces. The boundary layer refinement allows to accurately resolve the concentration gradients and friction losses at these surfaces. The entire unit cell mesh is generated from mirroring the illustrated mesh at its two symmetry planes. The design of this mesh and its implementation in a blockMesh script is a significant part of this study. Its script is found in an example case in this repository (Aschmoneit, 2019a).

The cross flow through the channel is prescribed through the applied pressure gradient magnitude and orientation, see Fig. 3.4(a). Figure 3.4(b) illustrates how the spacer disturbs the flow through the channel. The streamlines are not uniform but show regions of turbulent eddies in the center, and wind shade effects where the spacer meets the membrane. The spacers' mixing characteristics are quantified in terms of the mass transfer coefficient k_d , and the pressure gradient ∇p applied to drive the cross flow at a given flow rate.

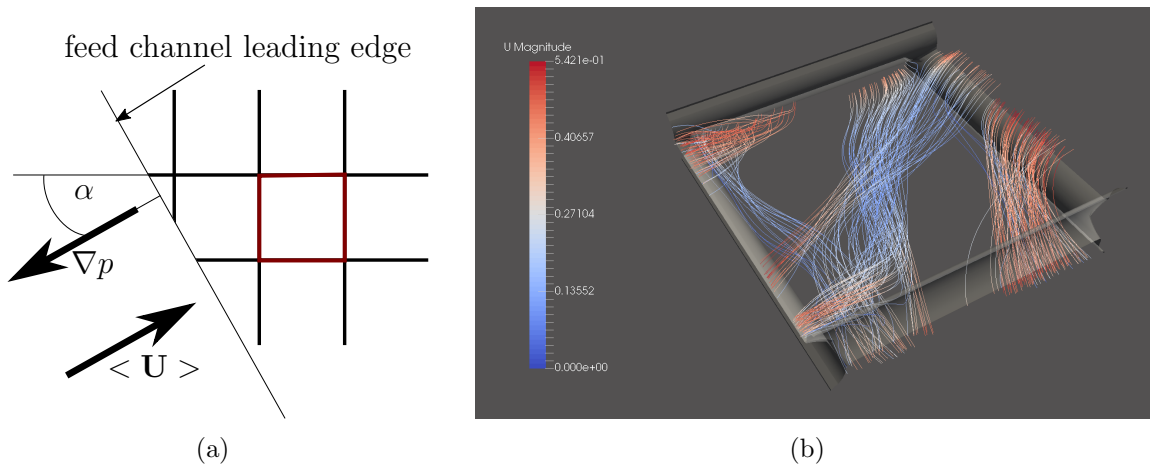


Figure 3.4: (a) Sketch of feed spacer grid with red unit cell. The pressure gradient ∇p defines the incident angle, i.e. the spacer orientation, α , and the cross flow magnitude $\langle U \rangle$. (b) Snap shot of developed cross flow with $\alpha = 30^\circ$. The simulation parameters are found in **IV**.

The mass transfer coefficient is defined analogously to the heat transfer coefficient, as the ratio of the solute concentration surface normal gradient, and the difference of the solute concentration between the surface and the bulk, multiplied with the solute diffusion coefficient D :

$$k_d = \frac{\partial_n c|_0}{\Delta c} D \quad (3.1)$$

As this coefficient is not a standard quantity in OpenFOAM its implementation to OpenFOAM is a key component of this study, whose source code is found in (Aschmoneit, 2018). Figure 3.5 shows maps of the local mass transfer coefficient, for different spacer orientations α in a top-down perspective of the bottom membrane. The general flow direction is defined by the spacer orientation and indicated by the black arrows in the top left corners. The local flow is illustrated by the streamlines, which originate from the two upstream periodic surfaces, i.e. the left and bottom

edge in this perspective. The pressure gradient magnitude, and hence the mean cross flow velocity, is similar in all cases.

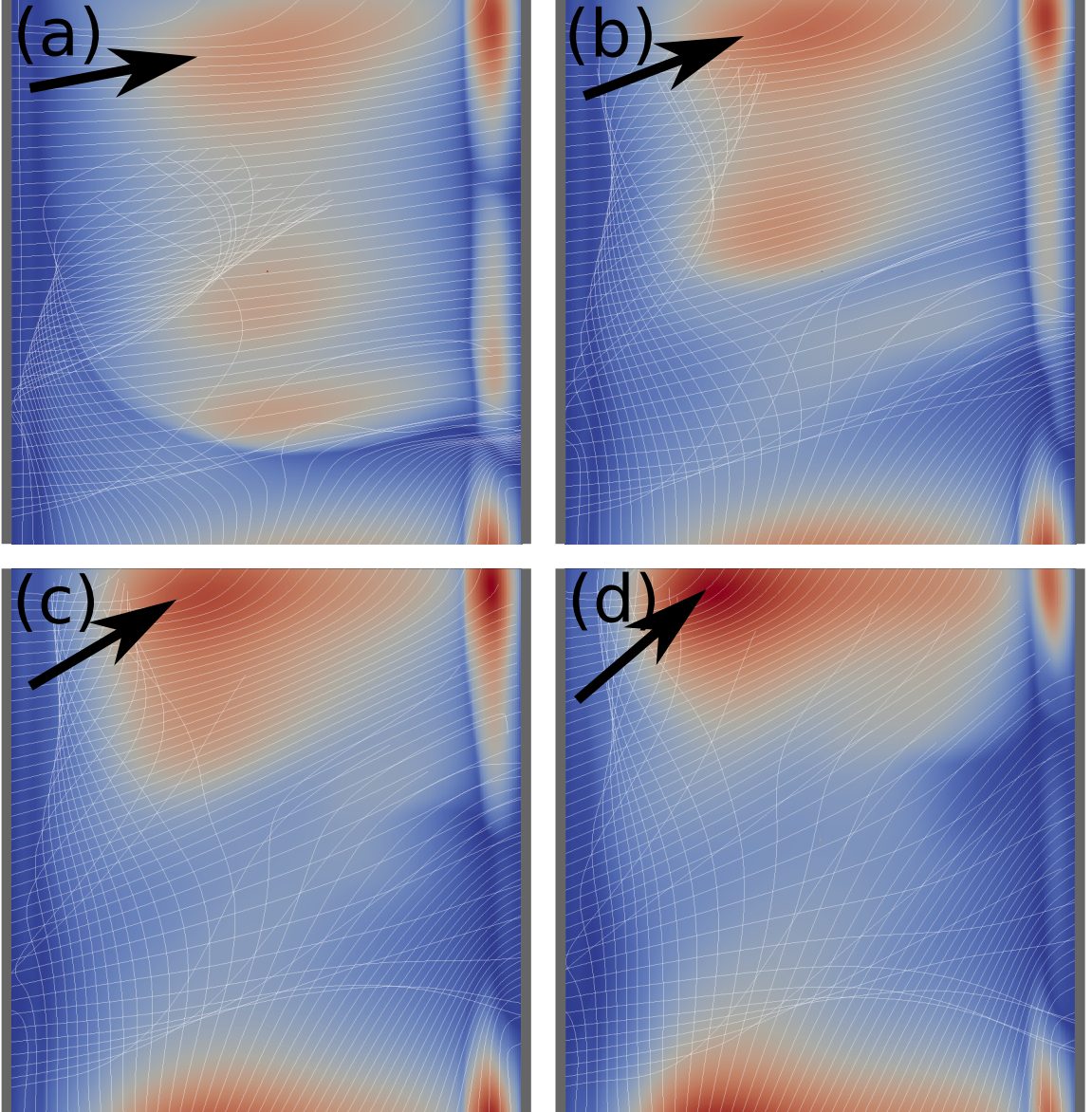


Figure 3.5: Mass transfer coefficient k_d of bottom membrane for spacer orientations (a) 10°, (b) 20°, (c) 30°, and (d) 40°. Red indicates high local mass transfer. The simulation parameters are found in **IV**.

Concentrative ECP can be defined as the inverse of the mass transfer coefficient. Hence, blue regions in Fig. 3.5 represent areas with high ECP and therefore low

local water flux. The earlier described wind shade effects can also be seen in the mass transfer maps along the left edges, where the spacer obstructs the flow and steep concentration gradients evolve. In general, the variance of the mass transfer increases with the flow incident angle.

The spacers' solute mixing characteristics are quantified by the mean mass transfer coefficient over the top and bottom membrane and expressed through the dimensionless Sherwood number:

$$Sh = \frac{k_d d_h}{D} \quad (3.2)$$

Figure 3.6 shows the results of the CFD simulations, where the mass transfer was measured for various cross flow velocities and spacer orientations, for the d28m spacer geometry on the left, and the d34m geometry on the right. For all orientations an increased cross flow velocity causes better solute mixing, increases the mean mass transfer and hence the water permeation. It is also seen that increasing the incident angle α , see Fig. 3.4(a), has a positive effect on the mean mass transfer coefficient. However, this effect diminishes as $\alpha \rightarrow 40^\circ$.

In order to comprehend the underlying physics of mass transfer and pressure drop, the CFD data set is quantified in terms of a scaling law, in which the spacer orientation dependence is expressed through the sine term, and the two different spacer geometries are incorporated through the hydraulic diameter term:

$$\Psi = [c_1 + c_2 |\sin(2\alpha)|] \left(\frac{d_h}{l} \right)^{c_3} Re^{c_4}, \quad (3.3)$$

The least square fit of the combined data sets yields the scaling coefficients as:

$$Sh = [2.35 + 0.57 |\sin(2\alpha)|] \left(\frac{d_h}{l} \right)^{-0.44} Re^{0.49} \quad (3.4)$$

The lines in Fig. 3.6 are plots of this scaling relation. The scaling of the Reynolds number quantifies the positive effect of increasing cross flow. The orientation dependence is well-captured by the sine term in equation (3.4). The mean mass transfer is increased significantly by $\sim 24\%$ for a 45° feed spacer orientation.

Similarly, the pressure drop is quantified through the Darcy-Weisbach equation:

$$f = \frac{2d_h \partial_x p}{\rho u^2}, \quad (3.5)$$

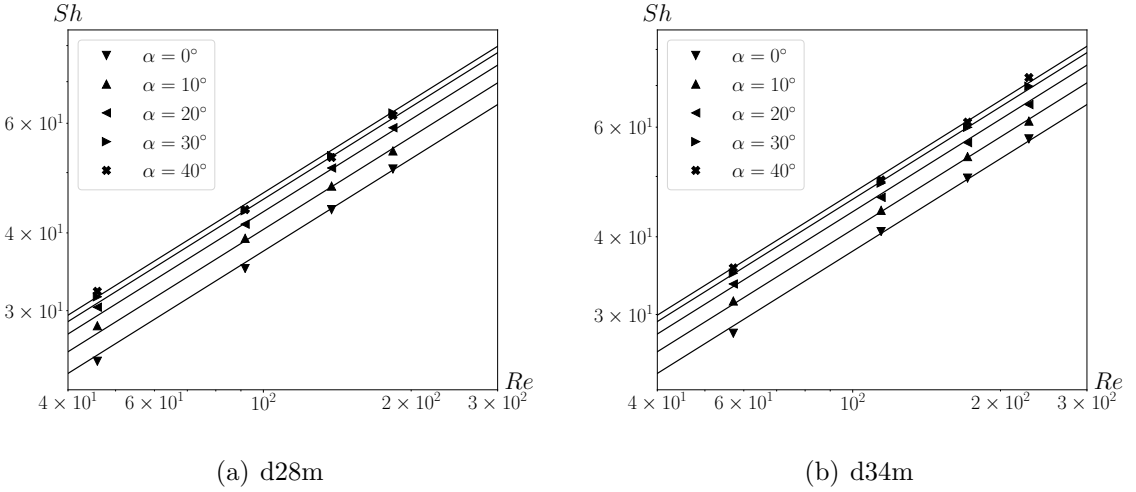


Figure 3.6: Mass transfer data and scaling relations. Both, the cross flow, and the spacer orientation affect the mass transfer.

where f is the Darcy friction factor, ρ is the fluid density, and u is the mean cross flow velocity. Figure 3.7 shows the pressure drop in terms of the friction factor against the cross flow for the d28m spacer (left) and the d34m spacer (right). Similar to the mass transfer data, the friction factor increases with increasing incident angle α . The data is subjected to the same power law (3.3) template whose least square fit yielded the power law scaling as:

$$f = [26.16 + 4.95|\sin(2\alpha)|] \left(\frac{d_h}{l}\right)^{0.72} Re^{-0.49} \quad (3.6)$$

The low cross flow data points, see red ellipses in Fig. 3.7, were discarded in the least square fitting. It will have to be investigated why these data points don't scale similarly to the others. One possible explanation could be that the spacers induce turbulent flow at lower Reynolds numbers, compared to pipe flow, for which different scaling laws apply to laminar and turbulent flow. However, the scaling relation is well supported by the remaining data points. The solid lines in Fig. 3.7 show the plots of equation (3.6) and illustrate the conformity of the fit and the data. A $\sim 19\%$ increase of the pressure drop is caused by a 45° feed spacer orientation.

The scaling analysis on the two spacer geometries quantifies the extend to which the spacer orientation increases both, the mass transfer coefficient, and the pressure drop. In order to evaluate the significance of these effects on the module scale, a simplified water flux model is presented and applied to three different RO processes. Assuming an ideal membrane without solute leaking, and negligible pressure in the

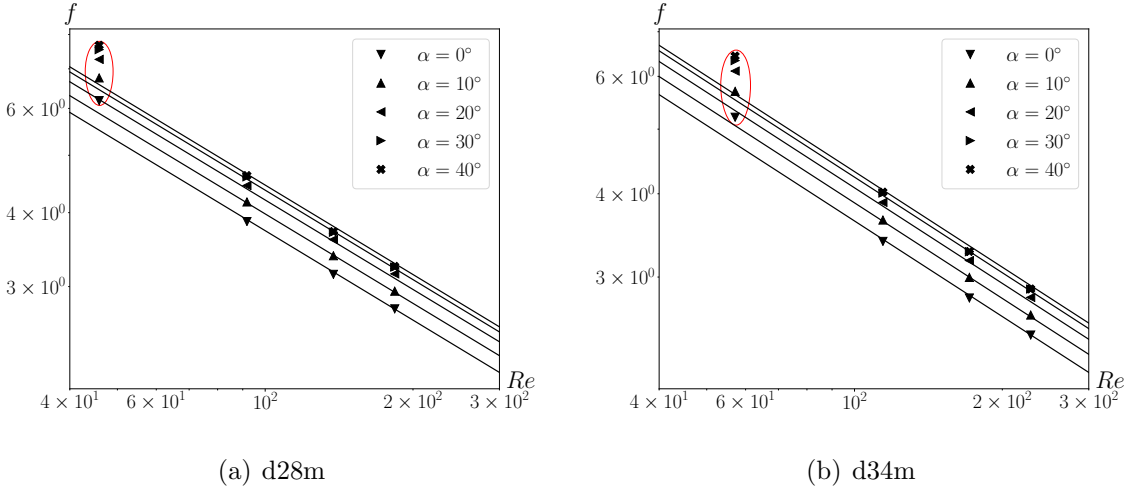


Figure 3.7: Pressure drop data and scaling relation against cross flow and spacer orientation. The low velocity cross flow data samples, indicated by red ellipses, are not scaling in the same way as the remaining data set. They are discarded from the scaling analysis.

permeate channel, the RO water flux equation (2.7) reduces to:

$$j_w = A(p_f - \pi_{a,f}) \quad (3.7)$$

Because of concentrative ECP the solute concentration at the membrane is greater than in the bulk, $\pi_{a,f} > \pi_f$. This concentration difference can be expressed through the geometry's mass transfer coefficient (Mulder, 1991).

$$c_{a,f} = c_f \exp\left(\frac{j_w}{k_d}\right) \quad (3.8)$$

The resultant water flux equation is:

$$j_w = A \left[p_f - \pi_f \exp\left(\frac{j_w}{k_d}\right) \right] \quad (3.9)$$

Equation (3.9) is transcendental and must therefore be solved numerically. Assuming a membrane water permeation coefficient of $A = 3.7 \text{ l}/(\text{m}^2 \text{ h bar})$, and a cross flow velocity of $u = 0.2 \text{ m/s}$, the water flux equation (3.9) is solved for different filtration applications, and different hydraulic pressures p_f . The filtration applications are set as brackish water RO ($\pi_f = 5 \text{ bar}$), seawater RO ($\pi_f = 30 \text{ bar}$), and brine RO ($\pi_f = 55 \text{ bar}$). The applied range of hydraulic pressure depends on the respective osmotic pressure as $p_f \in [\pi_f, 2\pi_f]$. Figure 3.8(a) shows the gain of the relative water

flux by turning the feed spacer by 45° , against the normalized pressure $p'_f = p_f/\pi_f$, for the three filtration applications and the two spacer types. The two bottom curves refer to the d28m spacer (dashed curves) and to the d34m spacer (solid curves), for the brackish water application. Due to the low solute concentration, the effect of a 45° oriented spacer is marginal, yielding an approximate 1% improvement compared to the flow-aligned spacer orientation. However, the filtration applications with high solute concentrations show a significant water flux increase, due to the spacer orientation: For seawater RO a water flux increase of up to 6%, and for brine RO of up to 10%, are reached. For all three applications alike, the bigger d34m spacer yields a slightly greater water flux.

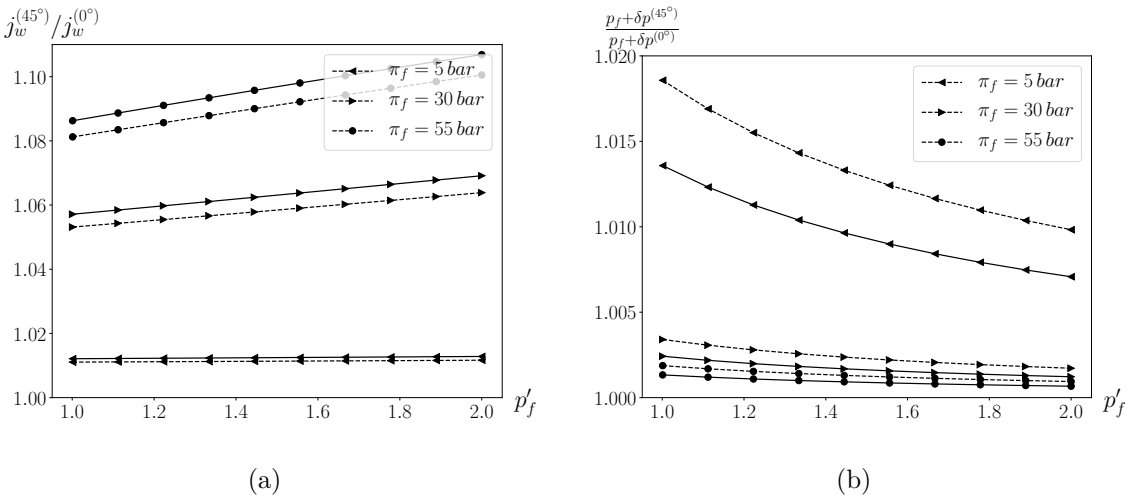


Figure 3.8: (a) Relative gain of water flux with 45° oriented feed spacer, for different feed osmotic pressures, and two spacer types (d28m is represented by dashed curve, and d34m by solid curve): The water flux increase is more significant for more saline applications. (b) Relative increase of total pressure with 45° oriented feed spacer: The increase of the pressure drop is significant for brackish water RO.

The significance of the spacer orientation for the pressure drop is analyzed with respect to the total applied pressure, i.e. the hydraulic pressure p_f and the driving pressure δp . A module length of 1 m was assumed for this analysis, which closely resembles the dimensions of the 8040 SWM type. Figure 3.8(b) shows the relative increase of total applied pressure. The two top curves refer to the brackish water RO case which indicate a relative increase of total pressure between 1% and 2%. Relating this to the corresponding water flux increase of only $\sim 1\%$, it does not compensate for the pressure drop increase. For the two other filtration applications, on the other hand, the relative total pressure increase is less than 0.4%, while their

water flux increase lies between 5% and 10%. This indicates a significantly higher efficiency of the 45° feed spacer orientation.

This study quantifies the effect of the feed spacer orientation on the filtration rate and the pressure drop in SWMs. It can be concluded that for seawater and brine RO, the filtration rate in SWMs is significantly improved, while the total pressure increase is insignificant. For brackish water RO, the significant pressure increase annihilates the only marginal water flux increase.

This study will be continued with a comparison to experimental data on the SWM pressure drop. Furthermore, the scaling analyses will be extended to non-orthogonal, diamond shaped spacer-types.

3.2 Upscaling reverse osmosis: Efficient designs for desalination plants

The design of effective RO desalination systems is a complex challenge. For a given target filtration rate and purity, the system efficiency depends on the available feed stream flow rate and salinity, the embedded SWM elements, and the operation- and investment costs. The operation- and investment costs are governed by the system design, i.e. the amount of SWMs, their configuration, and the system operation, in terms of feed flow rates and applied pressures.

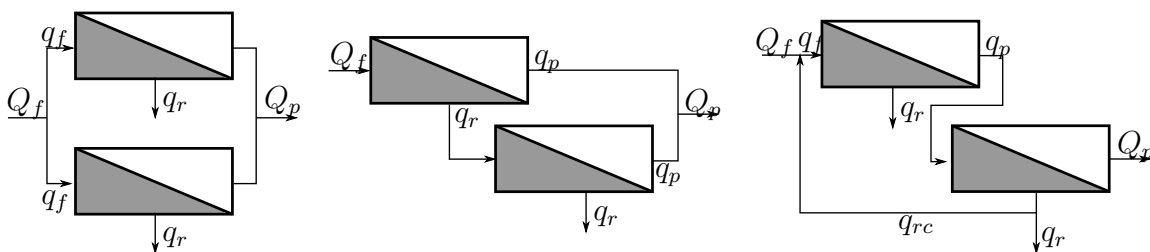


Figure 3.9: Fundamental module configurations: single-pass *SP_2* (left), retentate-staging *RS_1.1* (middle), permeate-staging with recirculation *PS_1.1* (right). Q denotes a system flow rate and q denotes a module flow rate. The subscripts f , r , p and rc stand for *feed*, *retentate*, *permeate* and *recirculation*, respectively.

Figure 3.9 illustrates three fundamental configuration concepts which the following, more complex configurations can be referred to. The left configuration is a single pass configuration with two parallel elements (*SP_2*). This configuration is preferred when the permeate stream has an acceptable purity and the total number of elements

should be minimized. The middle configuration is a retentate staging configuration (*RS_1_1*), in which the first stage's retentate acts as the feed for the second stage. This configuration is preferred when the combined permeate purity is acceptable and the operating costs should be minimized. In the right configuration the first stage's permeate acts as the second stage's feed (*PS_1_1*). This configuration is preferred when the first stage's permeate is not of sufficient purity and needs a second filtration stage. In the *PS* configuration the second stage's retentate is pressurized and has a lower salinity than the incoming feed stream. The second stage's retentate is therefore often recirculated to the feed stream.

The optimization of filtration plants is a complex problem. Different software tools have been developed for this task, such as *ROSA* (Dow(Du Pont), 2019), *TorayDS* (Toray, 2019), or *Winflows* (SUEZ Water Technologies and Solutions, 2019). These filtration plant design tools are usually free of charge, but are reduced the respective companies products.

This study introduces the OMSD (open membrane system design) tool for filtration system simulations. The simulation tool is capable of modeling the fundamental configurations described above, and their arbitrarily complex derivatives. Its open development allows for the implementation of generic SWM modules, utilizing arbitrary membranes, and the extension of the tool, to also simulate other filtration processes. In the following chapter, the OMSD's functioning is outlined. Thereafter, its application is demonstrated in two desalination problems. This chapter is based on **II**. An example case of the OMSD is found in this repository: (Aschmoneit, 2019c).

Figure 3.10 shows a screen shot of the OMSD with its components for the simulation of a *RS_1_1* system. These components are described in the following and more accurately described in **II**. With the feed source (A), the feed volume flow rate and its salinity are defined. Through the pre-treatment element (B), an energy demand for the feed stream pre-treatment is defined. The pump (C) pressurizes the stream and returns its energy demand. The stream probes (D) show the stream state, in terms of the volume flow rate, pressure, and solute concentration, at specified locations. The system efficiency is evaluated from the feed stream (D1), the permeate stream (D2), and the driving power of the pumps and pre-treatment. Most importantly, the RO SWM element (E) separates an incoming feed stream into a permeate stream and a retentate stream. Its filtration rate is defined as:

$$q_p = j_w A_m, \quad (3.10)$$

with the membrane area A_m . The water flux j_w is evaluated from the embedded membrane water permeation coefficient, and a mass transfer scaling relation, similar to the RO SWM study in chapter 3.1. The solute leaking is governed by the

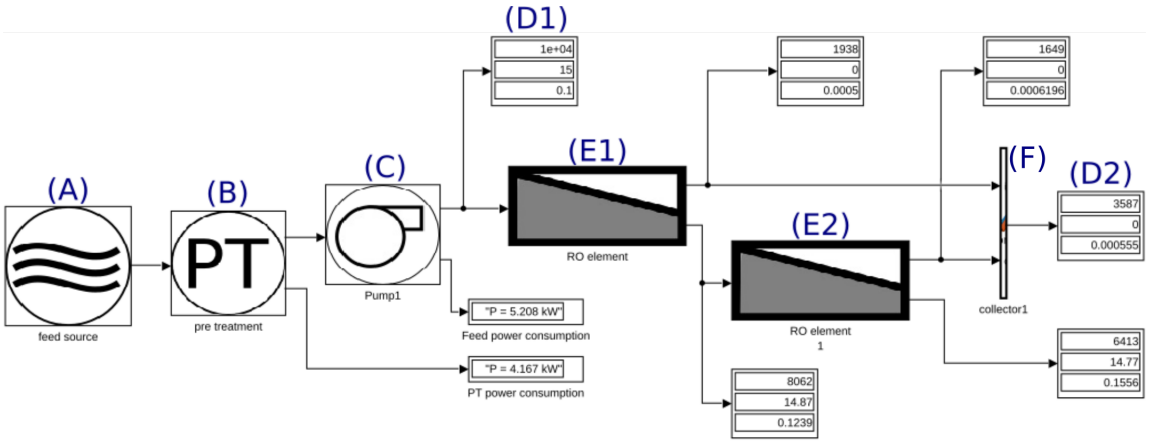


Figure 3.10: Screenshot of filtration system in *RS_1_1* configuration: (A) *Feed source*, (B) *Pre-Treatment* (C) *Hydraulic Pump*, (D) *Stream Probes*, (E) *RO SWM*, (F) *Stream Collector*

membrane's solute rejection coefficient R_s . Together with the feed flow rate and the permeate flow rate, the permeate solute concentration is defined as:

$$c_p = c_f(1 - R_s) \quad (3.11)$$

Finally, the pressure drop through the feed channel is defined through the Darcy-Weisbach equation (3.5), applied to a scaling relation for the fraction factor, similar to the RO SWM study in chapter 3.1.

OMSD application

The OMSD tool is demonstrated through the simulation of various configurations for two case studies which concentrate on potable water production from brackish water and brines. For both cases the only requirements are a water production rate of at least $400 \text{ m}^3/\text{d}$ and a drinking water purity of at most 1.7 mM NaCl . Only one SWM type is applied which has a water permeation coefficient of $A = 5 \text{ l}/(\text{m}^2 \text{ h bar})$, a rejection coefficient of 99.5%, and a total membrane area of 41 m^2 . Pumps are assumed to work at 80% efficiency.

Brackish water desalination

In this case study the salt concentration in water is assumed to be $c_f = 0.2 \text{ M}$. Because of this low concentration a single pass through a SWM already exceeds the target purity. Permeate staging configurations are therefore not considered in this application. Instead, different retentate-staging configurations are evaluated for their

capability in reaching the system requirements, for their energy demand per filtrated volume, and for the total number of utilized SWM. The considered configurations are (1) $RS_{3-3-3-3}$, (2) $RS_{3-3-3-3-3}$, and (3) $RS_{4-4-4-4}$. The notation of a configuration indicates the number of elements per stage which is repeated for every stage. This combination of configurations is chosen, because it allows to compare the effects of additional stages (through (2), (1)), and additional parallel trains (through (3), (1)).

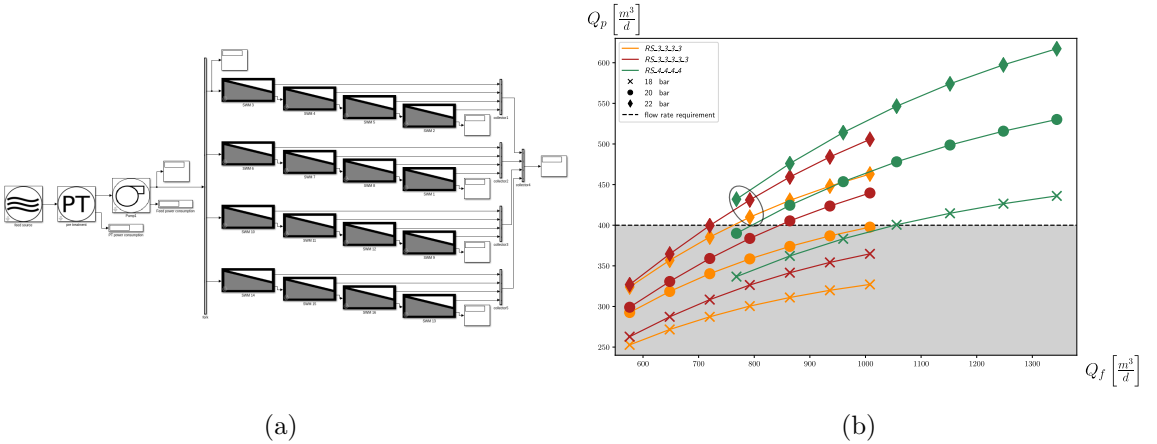


Figure 3.11: (a) System design export from *OMSD*: The $RS_{4-4-4-4}$ configuration for brackish water desalination. (b) Filtration rates of different configurations, under different operating conditions, for the brackish water desalination case. The dashed line shows the filtration rate requirement. The ellipse indicates the most energy-efficient operation modes, according to Fig. 3.12.

Figure 3.11(a) shows an illustration of the $RS_{4-4-4-4}$ simulation setup with four trains of four SWM each. The system configurations are tested for a range of operating conditions in terms of total feed inflow rate and applied feed pressure:

$$\begin{aligned} q_f &\in [192, 336] \frac{m^3}{d} \\ p_f &\in \{18, 20, 22\} \text{ bar} \end{aligned} \quad (3.12)$$

The feed inflow in (3.12) refers to the feed flow rate per first stage SWM. Figure 3.11(b) shows the total filtration rate for three different configurations, under operating conditions (3.12). The gray shaded area indicates insufficient water production rates. It is seen that all configurations can yield the target productions rate for certain operating conditions. The small $RS_{3-3-3-3}$ configuration only reaches the target flow rate when operated at 22 bar and with a reasonable high feed flow rate. Through adding another stage, i.e. configuration $RS_{3-3-3-3-3}$, the system already

yields the target filtration rate with 20 bar. The broader *RS-4-4-4-4* configuration yields the target filtration rate for almost all operating conditions.

For all configurations and operating conditions, that reach the target water production, the energy demand per m^3 produced water is calculated based on the pump- and pre-treatment energy consumption. Figure 3.12 shows the specific energy demand, indicating the significance of the applied operating conditions. For all configurations the most energy-efficient operation mode is the combination of a low feed flow rate and high feed pressure. The configurations' most efficient operation modes can be compared and related to the system size: Compared to the *RS-3-3-3-3* system, the *RS-3-3-3-3* system needs 5% less energy, at the expense of 25% more modules. Similarly, the *RS-4-4-4-4* system needs 10% less energy, but uses 33% more modules.

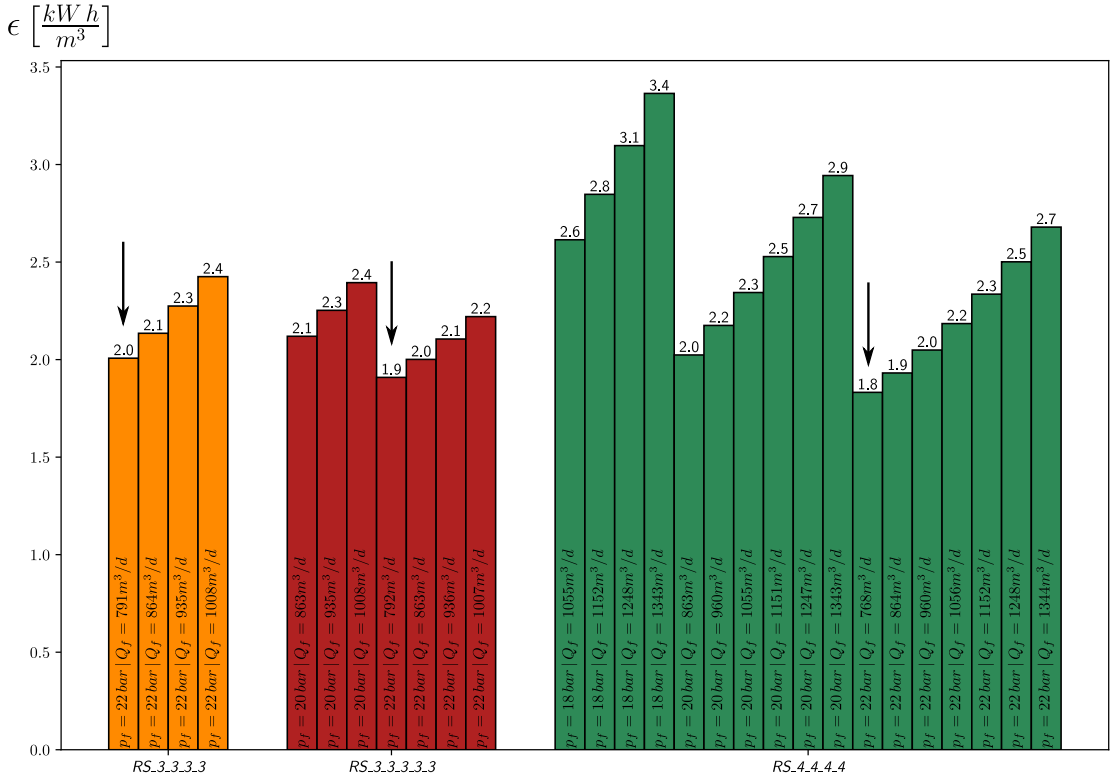


Figure 3.12: Specific energy demand for the three configurations and those operating conditions, that meet the filtration rate requirement, for brackish water desalination.

Brine desalination

The desalination of brines are more complex, due to the higher salt concentration: The target purity cannot be met in a single filtration pass. Therefore, only permeate-staging configurations are considered in this case study. The considered configurations all have two stages with different numbers of elements and different ratios of the number of elements in the first stage and in the second stage. Figure 3.13(a) shows an exemplary PS_{5-2} system. The second pump between the two stages pressurizes the first stage's permeate to act the second stage's feed. The second stage's retentate is recirculated to the system feed stream. The considered configurations are PS_{9-6} , PS_{12-3} , PS_{14-7} , and PS_{15-5} . In permeate-staging systems the driving pressure is set for both stages separately. The high feed salt concentration of $c_f = 1.5 M$ requires a high pressure in the first stage, which is defined as $p_f^{(1)} \in [60, 90] \text{ bar}$. In the second stage, the salt concentration is significantly lower, requiring a much lower driving pressure. In this case study the second stage pressure is adjusted to yield a 80% recovery in the first stage, which, in turn, defines the recirculation ratio. In the first stage are all configurations driven with feed flow rates of $q^{(1)} \in \{72, 108\} \text{ m}^3/\text{d}$ per element.

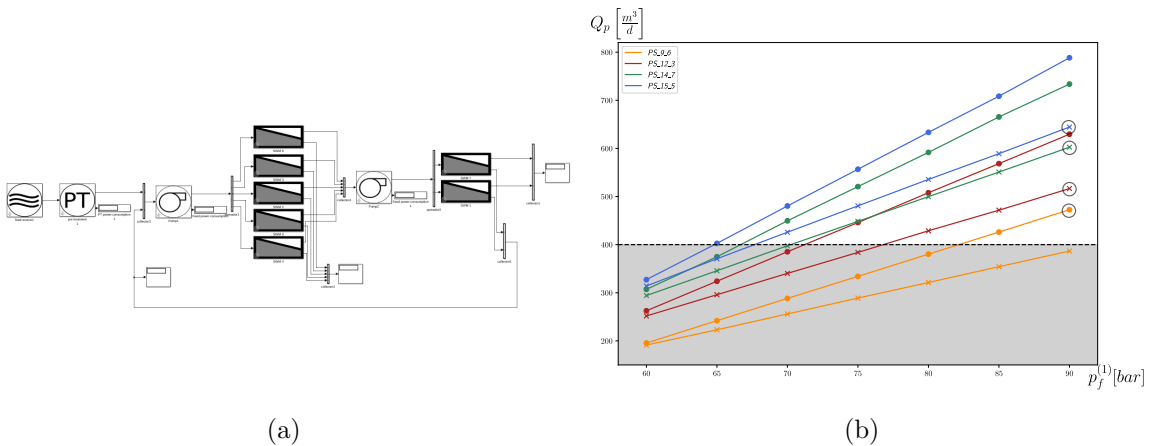


Figure 3.13: (a) System design export from *OMSD*: The PS_{5-2} configuration for brine desalination. (b) Filtration rates of different configurations, under different operating conditions, for the brine desalination case. The dashed line shows the filtration rate requirement. The circles indicate the respective most energy-efficient operation mode, according to Fig. 3.14.

Figure 3.13(b) shows the simulation results of the four configurations, for the two different feed flow rates, against the first stage feed pressure. It is seen that all configurations can reach the target water production for certain operating conditions.

Figure 3.14 shows the specific energy demand for those operating conditions that fulfill the filtration requirements. Similar to the brackish water RO, the most effective combination of operating conditions are low feed flow and high feed pressures. As a result of this system setup, these combinations of operating conditions yield the smallest recirculation ratio. The largest system (*PS_14_7*) provides the most energy efficient brine desalination. Compared to the most efficient *PS_12_3* system, the *PS_14_7* needs $\sim 10\%$ less energy, while using 40% more elements. A comparison of the equally sized *PS_9_6* and *PS_12_3* systems, reveals a $\sim 7\%$ reduced energy consumption of the *PS_12_3*.

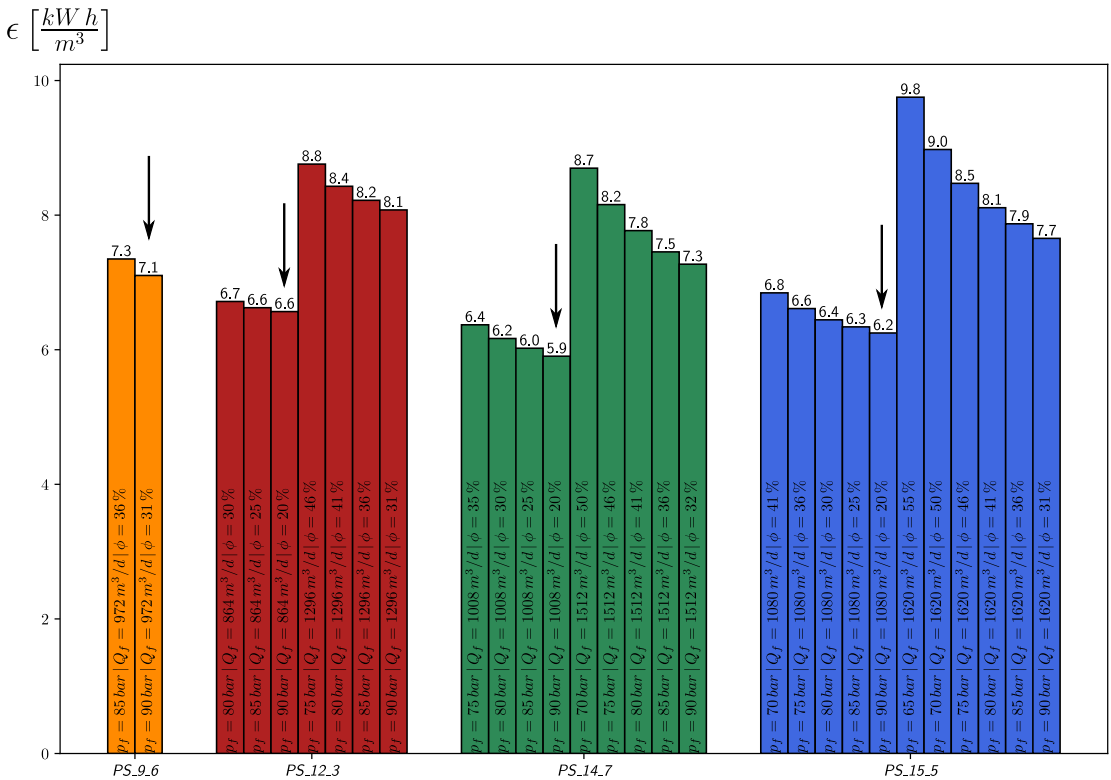


Figure 3.14: Specific energy demand for the three configurations and those operating conditions, that meet the filtration rate requirement, for brine desalination.

Ideal system designs and operations

The two desalination applications require two fundamentally different system design concepts, namely retentate-staging for low concentration desalination, and permeate-staging for high concentration desalination. Both concepts are most efficiently operated at low feed flow and high feed pressure. However, membranes operated at low

feed flow are more prone to membrane fouling, which sets a practical limit as to how low the feed flow may be. This effect is not simulated in the OMSD tool, but will be incorporated in its future development.

The analysis of different configurations shows that larger systems can reach a higher energy efficiency. However, this improvement comes at the costs of significantly more modules, and therefore greater investment costs. Efficient desalination plant design is therefore always a trade-off between operation- and investment costs. For a more precise simulation of desalination plants, the OMSD tool will have to also include pressure exchangers and PRO energy recovery systems.

4 Advancing osmosis-driven membrane technologies

Osmosis-driven membrane processes refer to FO, PRO, and PAO, see Fig. 2.3. PAO enhances the FO permeation rate through a hydraulic pressure on the feed side, and is therefore not energy-neutral and not considered in this thesis. FO is an advancing membrane process which can be used as a stand-alone technology with applications in e.g. the food industry for producing concentrates, or as a hybrid process for dewatering wastewater streams, before a subsequent RO filtration. Since FO is a pressure-less, natural process, it is potentially very energy efficient and has a low fouling propensity. The hollow fiber module (HFM) is a promising module type for FO applications. Its dominant design feature, i.e. the fibers' packing density, is investigated in Chpt. 4.1. PRO is an energy generation process, in which the osmotic permeation into the pressurized draw channel creates a pressurized net flow, which is led to a hydro turbine. It could be applied as a stand-alone technology for e.g. seawater as the draw stream, or as a hybrid process in combination with RO, acting as an energy recovery system. PRO is not widely commercialized, which is also due to the lack of PRO-specific module designs. In Chpt. 4.2 a novel design for PRO is introduced and its energy generation efficiency assessed.

Typical ODMP applications are operated in cross flow configurations, in which draw and feed streams are constantly lead over the membrane. This allows a continuous operation of the membrane. Fig. 4.1 shows a sketch of how an ODMP module is operated: The flow stream state is defined by the three quantities volume flow rate Q , hydraulic pressure p , and osmotic pressure π . As depicted in Fig. 2.2 the ODMP are defined by the osmotic pressure difference exceeding the hydraulic pressure difference, $p_d - p_f \leq \pi_d - \pi_f$, which causes the osmotic volume flow rate δQ into the draw side. The consequent dilution of the draw stream leads to a lower osmotic pressure in the draw out-stream, $\pi'_d < \pi_d$. Likewise, the feed stream is upconcentrated, $\pi'_f > \pi_f$. Both streams are driven by hydraulic pressure, which causes pressure losses δp in both channels. An efficient ODMP exhibits a high osmotic flow rate δQ , at low driving pressures δp .

In ODMP the water flux is directed towards the draw side, while the salt leaking allows for the diffusion of salt through the membrane towards the feed side. This reverse salt flux contaminates the seed reservoir and significantly reduces the water permeation rate through ICP, see Fig. 2.3. In order to reduce this effect, FO and

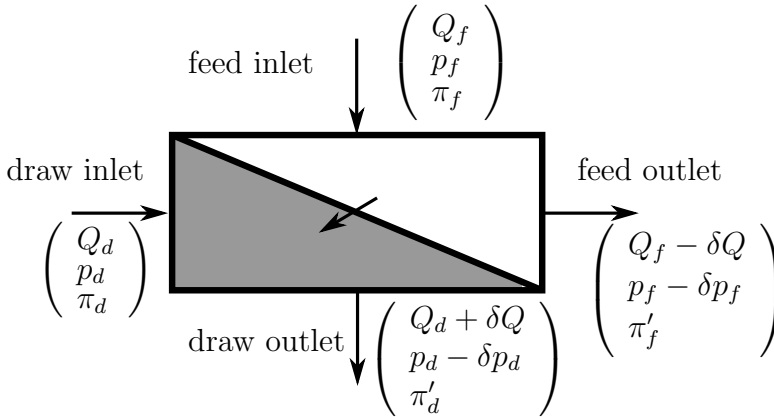


Figure 4.1: Schematics of ODMF with stream states at inlets and outlets. FO is defined through $p_d = p_f = 0$, and most PRO applications have negligible feed osmotic pressure and are defined through $\pi_d - p_d > 0$, $p_d > 0$. ODMFs are optimized through maximizing δQ , while minimizing δp_d .

PRO membrane development concentrates on lowering the membranes' salt permeation coefficient and the thickness of the structural support.

Another dominating effect limiting the water flux in ODMF is the dilutive ECP on the draw side. This problem is met by mixing the draw solution, so that the solute concentration at the membrane surface is kept as high as possible, minimizing the local dilution. The draw solute mixing through hydrodynamic considerations is one major task of the membrane module design. Another important aspect of membrane module design is the operation pressure drop, which relates directly to the operation costs. Usually, an improved draw solute mixing causes an increased pressure drop. Therefore, a compromise between solute mixing and pressure drop must usually be found.

4.1 Optimized packing density of hollow fiber modules for forward osmosis

The most significant design parameter in HFMs is the packing density of the fiber bundle. It defines the total membrane surface area, which, in turn, affects the total water flux. On the other hand, the packing density defines the void space in the draw channel. For a given operation draw flow rate the void space defines the cross flow velocity through the shell side. The pressure drop over the draw scales approximately with the square of the cross flow velocity. In (Günther, Schmitz, Albasi, and Lafforgue, 2010) a CFD analysis on the effect of the packing density is conducted.

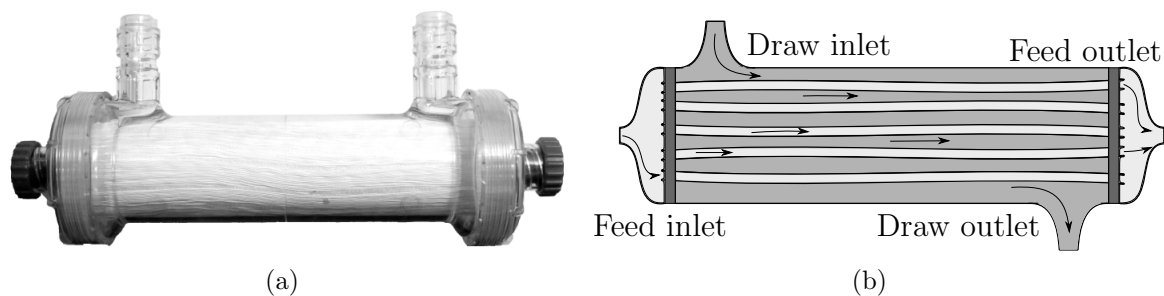


Figure 4.2: (a) Photo of a HFM indicating the fiber packing density. (b) Schematic illustration of HFM indicating the flow pattern.

It is concluded that an increasing packing density yields a non-uniform water flux distribution, and that the filtration flux decreases for high packing densities. The effect on the pressure drop was not included in this study.

This study quantifies in how far the packing density affects the total osmosis flow rate and the pressure drop over the draw channel. In order to analyze the effect of the packing density, a simplified CFD model is developed. It simulates the flow through the HFM shell side, under the effect of membrane water permeation and solute dilution. This chapter is based on **I** and an example case is published in (Aschmoneit, 2019b).

The HFM geometry is simplified by considering symmetry planes in the HFM. If the HF are assumed straight and arranged in a regular hexagonal array, the presence of neighboring fibers can be modeled by symmetry boundary conditions, see Fig. 4.3(a). Furthermore, the six symmetry planes in a hexagon can also be used to simplify the geometry to a dissected wedge shape. It is further assumed that the hydrodynamics in the feed channel, i.e. inside the fibers, do not affect the membrane flux significantly. The fiber lumen side does therefore not need to be resolved in the computational domain. Thus, under these assumptions the computational domain of the HFM is greatly reduced, see Fig 4.3(b). The domain is defined by the outer radius of the fiber R_1 , and the half-distance to the next fiber d . The packing density is then given by

$$\gamma = \frac{R_1^2}{d^2} \quad (4.1)$$

The resolution of the computational mesh is greatly increased towards the membrane surface, in order to resolve the concentration gradient in the boundary layer (ECP) sufficiently. The membrane water flux is modeled by a boundary condition which defines the local water flux as a function of the ECP-affected membrane surface

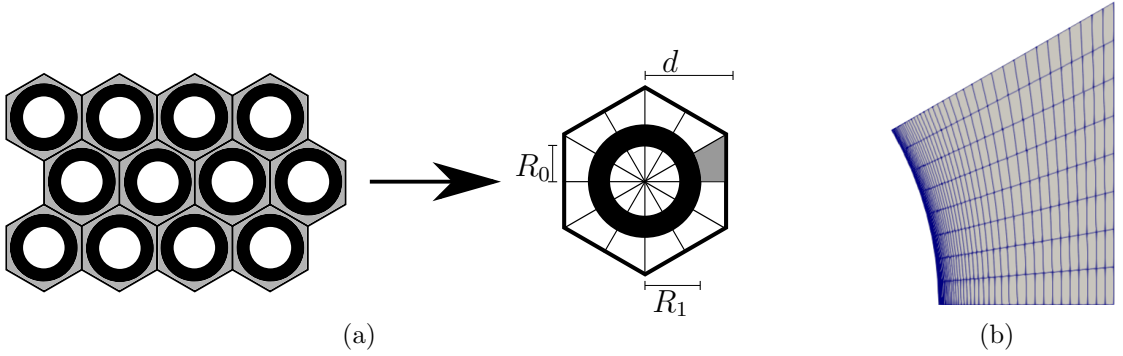


Figure 4.3: (a) Simplification of computational domain: If the fibers are assumed to be hexagonally arranged, the computational domain can be reduced to the gray area in the middle picture, by applying symmetry- and periodic boundary conditions. (b) Cross section of reduced HFM computational domain. ECP-induced steep gradients of salt concentration are resolved through the increased resolution towards the membrane surface. The packing density is defined through $\gamma = R_1^2/d^2$.

concentration, the membrane characteristics, and the fiber geometry. Because HFs are not flat, the assumption of constant fluxes throughout the support layer in the derivation of the FO water flux equation (2.11) doesn't hold. The local solute flux, is a function of the radial coordinate r . The solute transport equation for HFs therefore reads as:

$$J_s(r) = c(r)u(r) - \epsilon D \partial_r c(r), \quad (4.2)$$

Analogously to solving for the flat sheet water flux equation (2.11), the HF convection-diffusion equation (4.2) is solved in \mathbf{I} , yielding:

$$j_w = \frac{\epsilon D}{R_0 \ln \left(1 + \frac{\delta \tau}{R_0} \right)} \ln \left(\frac{A \pi_{s,d} + B}{A \pi_{a,f} + B + j_w} \right) \quad (4.3)$$

By comparison of the water flux equations (2.11) and (4.3), it is seen that they only differ in their geometric pre-factor. In the case of the HFs the water equation depends on the support parameters thickness δ , porosity ϵ , tortuosity τ and inner radius R_0 , while these parameters are condensed to the structural parameter S in the flat sheet case. In the CFD model the HF is modeled as a non-uniform flow inlet boundary condition along the HF surface. The local volume flux at the outer HF surface is related to the membrane flux equation (4.3) through:

$$u(R_1) = j_w \frac{R_0}{R_1} \quad (4.4)$$

The solute flux at the outer HF surface then follows as:

$$J_s(R_1) = j_s \frac{R_0}{R_1} \quad (4.5)$$

The boundary condition for the solute concentration then follows from the convection-diffusion equation and the opposing fluxes of water (4.4) and solute (4.5). Other surfaces in the computational domain were modeled as an inlet and outlet, generating the cross flow, and as symmetry boundary conditions, mimicking the effect of neighboring HFs.

Model validation

The CFD model is verified through comparison with experimental data obtained from (Ren and Mccutcheon, 2017). In order to resemble the experimental HFM, the following set of parameters were implemented in the computational HFM model:

Table 4.1: Benchmark test parameters

| Parameter | Symbol | Value | Unit |
|--------------------|------------|-------|-----------------|
| Geometry | | | |
| inner fiber rad | R_0 | 453 | μm |
| outer fiber rad | R_1 | 233 | μm |
| module rad | R_M | 12 | mm |
| module length | L_M | 0.457 | m |
| packing density | γ | 0.385 | - |
| Membrane | | | |
| water permeability | A | 0.45 | $l/(m^2 h bar)$ |
| solute permeation | B | 0.49 | $l/(m^2 h)$ |
| porosity | ϵ | 0.41 | - |
| tortuosity | τ | 1 | - |

The average module water flux j_w is measured against the draw concentration. Its relative deviation from the experimental data is defined as:

$$\sigma = \frac{j_w^{CFD} - j_w^{EXP}}{j_w^{EXP}} \quad (4.6)$$

Figure 4.4 shows the experimental flux data, together with the computational prediction and its deviation. It can be seen that the CFD model is in excellent agreement with the experimental data for solute concentrations of $c_d < 0.85M$. For greater concentrations the model produces a significant error, which might be related to the decreasing validity of the underlying van 't Hoff equation (2.6).

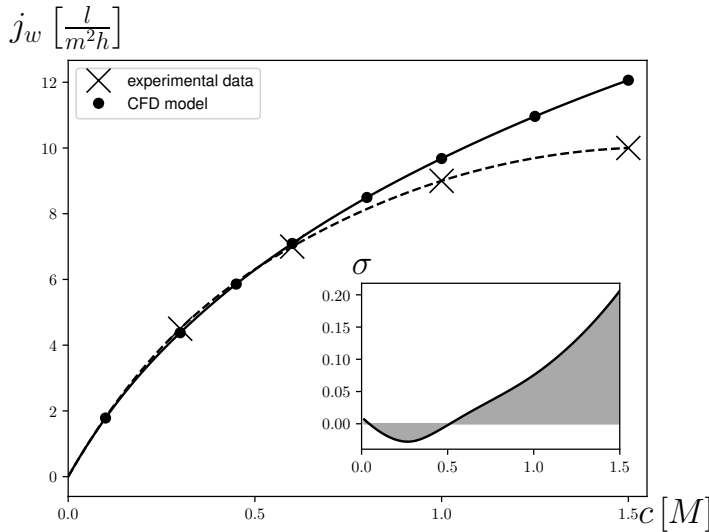


Figure 4.4: The CFD model is in excellent agreement with the experimental data for solute concentration of up to $c_d < 0.85M$. At higher concentrations the CFD model overpredicts the permeation rate.

The effect of the packing density on FO performance

The CFD model is executed on a module similar to the validation analysis module, with the exception of a wider module radius, $R_1 = 30 \text{ mm}$, see table 4.2. The average module water flux j_w is measured against the packing density γ , for three different combinations of operating conditions.

Figure 4.5 visualizes the effect of the packing density on the solute dilution. For the **C1.0Q100** configuration the figure shows the map of solute concentration at the module cross section, close to the module outlet, for the packing densities $\gamma = 80\%$ (left) and $\gamma = 20\%$ (right). It is clearly seen that the tight packing of the fibers causes a severe solute dilution and mutual ECP. The fibers are not optimally utilized and don't yield their maximum water flux. The loosely packed module, on the other hand, shows a low dilution level.

Figure 4.6(a) shows the average HFM water flux for the configurations in table 4.2, against the packing density. For comparison, the water flux values are normalized with the respective flux at $\gamma = 50\%$. The two configurations shown in Fig. 4.5 are indicated by arrows in Fig. 4.6(a). It is seen that the average water flux is greater in the high packing density configuration, although the concentration map indicated severe mutual ECP. The greater water flux in the $\gamma = 80\%$ configuration is attributed to the much higher cross flow velocity. Nevertheless, Fig. 4.6(a) indi-

Table 4.2: Parameter set for packing density analysis

| Parameter | Symbol | Value | | | Unit |
|--------------------|------------|-----------------|-----------------|----------------|-----------------|
| | | C1.0Q100 | C0.5Q100 | C1.0Q50 | |
| Geometry | | | | | |
| inner fiber rad | R_0 | 453 | 453 | 453 | μm |
| outer fiber rad | R_1 | 233 | 233 | 233 | μm |
| module rad | R_M | 30 | 30 | 30 | mm |
| module length | L_M | 457 | 457 | 457 | mm |
| Membrane | | | | | |
| water permeability | A | 0.45 | 0.45 | 0.45 | $l/(m^2 h bar)$ |
| solute permeation | B | 0.49 | 0.49 | 0.49 | $l/(m^2 h)$ |
| porosity | ϵ | 0.41 | 0.41 | 0.41 | - |
| tortuosity | τ | 1 | 1 | 1 | - |
| Operation | | | | | |
| draw flow rate | Q_d | 100 | 100 | 50 | l/h |
| draw concentration | c_d | 1.0 | 0.5 | 1.0 | mol/l |

cates that there exists a non-trivial maximum average water flux at $\gamma_{max} \approx 60\%$ for **C1.0Q100** and **C0.5Q100** and $\gamma_{max} \approx 45\%$ for **C1.0Q50**. Comparing the three configurations clearly shows that the module draw flow rate Q_d is the governing operation parameter for the maximum water flux yielding packing density.

As indicated in the chapter introduction, and symbolized by Fig. 4.1, is the module performance based on the absolute permeation flow rate δQ and the corresponding draw stream pressure drop δp_d . The absolute osmosis flow rate can be calculated from the average water flux and the module's geometry parameters through equation (4.7), see **I**:

$$\delta Q = \underbrace{J_w \frac{R_0}{R_1}}_{\text{flux at } R_1} \underbrace{2\pi R_1 h}_{\text{HF srf area}} \underbrace{\gamma \left(\frac{R_M}{R_1}\right)^2 \frac{\pi}{6 \tan(30^\circ)}}_{\text{number of HFs}} \quad (4.7)$$

Figure 4.6(b) shows the osmotic flow rate and the corresponding pressure drop against the packing density. Although the water flux in Fig. 4.6(a) shows a declining flux as $\gamma \rightarrow 1$, the increasing membrane area counteracts the flux decline and the absolute osmotic flow rate δQ increases as $\gamma \rightarrow 1$. By comparing the three configurations, one sees that the draw concentration has a much greater effect on the osmotic flow rate than the draw flow rate. The pressure drop, on the other hand, increases exponentially as $\gamma \rightarrow 1$, which makes very densely packed HFM inefficient. The pressure drop is not affected by the draw concentration. The two configurations

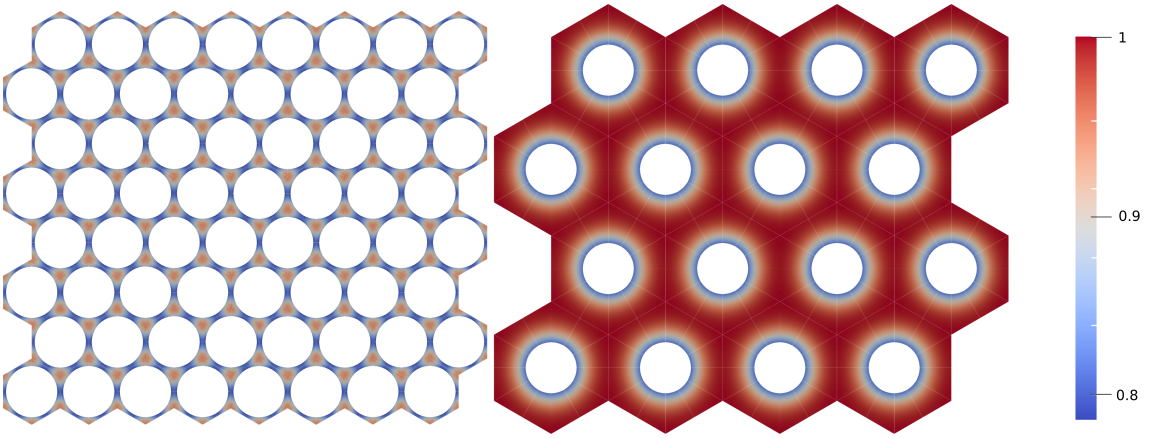


Figure 4.5: Map of draw concentration of draw channel for densely packed ($\gamma = 0.8$) and loosely packed ($\gamma = 0.2$) HFM: Tight packing yields great membrane surfaces but severe mutual ECP reduces HFM efficiency. Loose packing might not utilize the draw channel efficiently.

C1.0Q100 and **C0.5Q100** therefore have a similar pressure drop graph. Based on Fig. 4.6(b), a packing density of $\gamma \approx 0.7$ seems to be a reasonable compromise between osmotic flow rate and pressure drop.

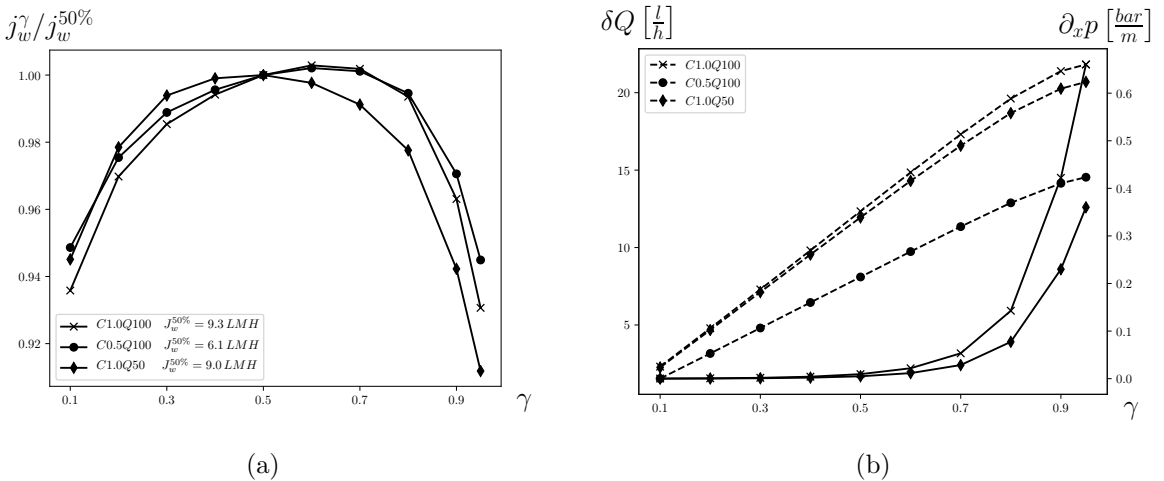


Figure 4.6: (a) Normalized water flux against the packing density, for different operation conditions. The two arrows indicate the two configurations in Fig. 4.5. (b) Absolute permeation flow rate and pressure drop against module packing density.

Despite the high level of abstraction and simplification, this CFD model can ac-

curately describe the osmotic flow in HFM for salt concentrations of $c_d \leq 0.85M$. It is shown how the packing density and the operation parameters affect the permeation flow rate and the pressure drop. An ideal packing density of $\gamma \approx 0.7$ is suggested. This simplistic model is believed to be suitable for the presented packing density analysis. However, a refined model would be based on a more sophisticated concentration-osmotic pressure relation, substituting the van 't Hoff equation, and a model for the permeation flux decrease through membrane fouling. Furthermore, a more general geometry with chaotically packed fibers would improve the model accuracy.

4.2 Efficient green energy generation with pressure retarded osmosis

Energy generation through PRO is not widely commercialized, due to insufficient membranes and pressure exchangers, and due to the lack of PRO-specific module designs. In this study, a novel, PRO-specific module design is presented and its performance is evaluated through a CFD model.

The submerged-helical module (SHM) design aims at maximizing the permeation flow, at a low pressure drop. Its dominant design features are the helical membranes, which are submerged in the draw channel and aligned with the cross flow, see Fig. 4.7 (b). The membranes are designed as membrane envelope sheets (MES), in which a membrane double layer encloses a tricot spacer, acting as the feed channel, see Fig. 4.7 (a). The twisted sheets deflect the cross flow in the membrane vicinity which affects the boundary layer over the membrane surface. The draw flow is therefore not perfectly parallel, although the general flow direction is defined by the module inlets and outlets. Through these inflicted flow disturbances the solute boundary layer gets locally minimized, which minimizes ECP and increases the membrane water permeation. As the membranes are twisted around their longitudinal axes, the SHM has a low membrane surface-per-volume ratio, which causes only a small pressure drop along the module draw channel.

Another consequence of the low packing density is the great draw volume flow rate necessary to operate the SHM with a sufficient cross flow velocity, and the low degree of dilution of the draw stream. This inefficiency is met by a draw stream bypass in the SHM system. Figure 4.8 shows the schematics of the draw side of a SHM system. The high pressure pump (P_{HP}) pressurizes the incoming draw stream to the operating pressure PRO operating pressure of $p_d \approx 0.5 \pi_d$ ¹. The booster pump

¹The power density in PRO is defined as: $P' = A\Delta p(\Delta\pi - \Delta p)$, which is maximized for $\Delta p =$

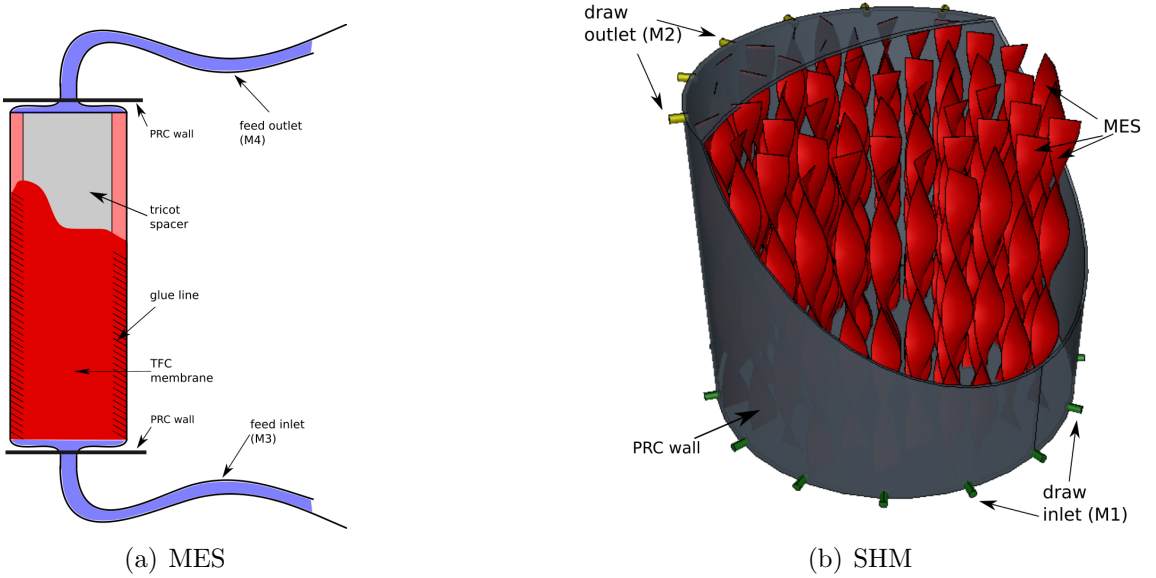


Figure 4.7: (a) Sketch of a membrane envelope sheet (MES): Two membranes in AL-DS configuration enclose a tricot spacer, which acts as the feed channel. (b) The MES are submerged in the pressure chamber (PRC), which feed inlets and outlets are traversed through the PRC walls.

(P_B) further pressurizes the stream to overcome the pressure drop in the SHM. As the draw stream is led through the SHM, (i) the pressure drops back to p_d , (ii) the osmotic permeation adds the flow rate δQ to the stream, and (iii) the stream is diluted. The share δQ of the stream is led to a hydro turbine (*TRB*), where a power of $\delta Q p_d$ is generated. The remaining share of the draw stream Q_d is led back to the bypass (*B*) or the pressure exchanger (*PX*). The bypass brings the share βQ_d back to the booster pump, while the remaining share $(1 - \beta)Q_d$ is used to pressurize the stream entering the system through the pressure exchanger. The bypass therefore determines how much of the slightly diluted draw stream is recirculated, compensating for the often low efficiencies of pressure exchangers.

This study (i) quantifies how the membrane twisting affects the pressure drop δp through a CFD model, and (ii) analyses how the recirculation parameter β affects the operation efficiency in terms of the net power generation. This chapter is based on **III** and the underlying CFD algorithm is found in (Aschmoneit, 2019d).

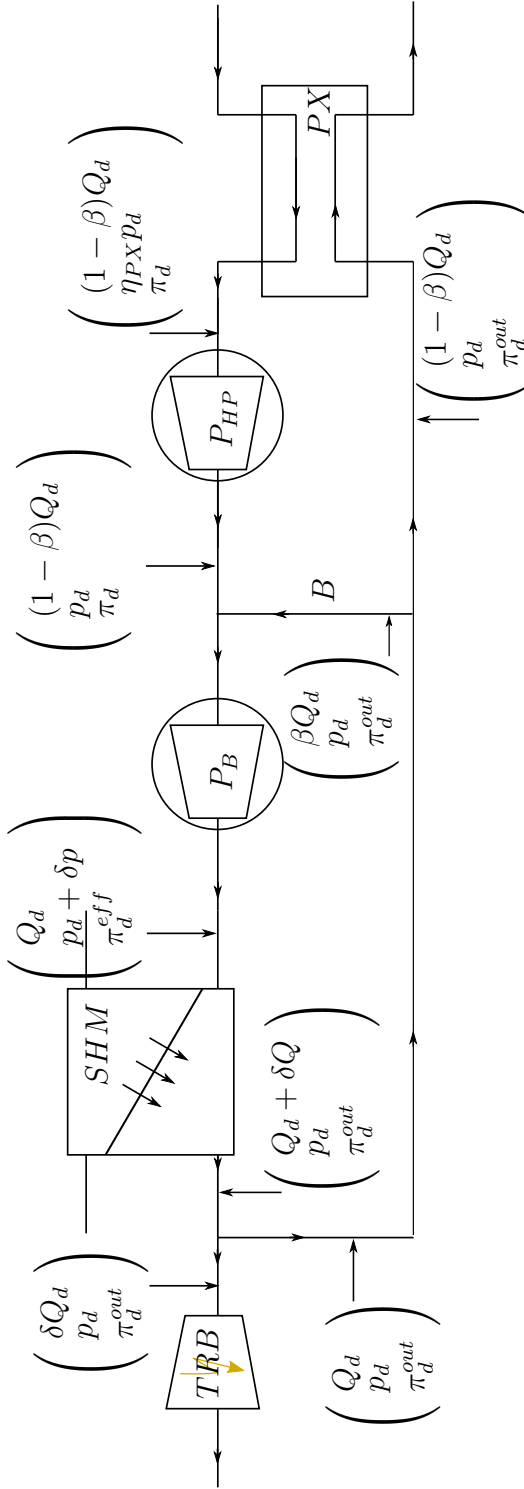


Figure 4.8: SHM-PRO system schematics of draw stream with hydro turbine (TRB), PRO module (SHM), booster pump (P_B), bypass (B), high pressure pump (P_{HP}) and pressure exchanger (PX). The state variables indicate the local flow rate, hydraulic pressure and osmotic pressure.

Mass transfer and pressure drop characterization

The CFD model is based on a simplified geometry, in which the MES are assumed to be arranged hexagonally. The geometry is reduced through the symmetry planes in the hexagonal matrix. Furthermore, the membrane itself is a non-planar symmetry boundary surface. The resulting computational domain is shown in Fig. 4.9(a). It defines the membrane (2) with width w_m and length l_m , the periodic boundaries (3), the symmetry planes (4) and the flow outlet (1).

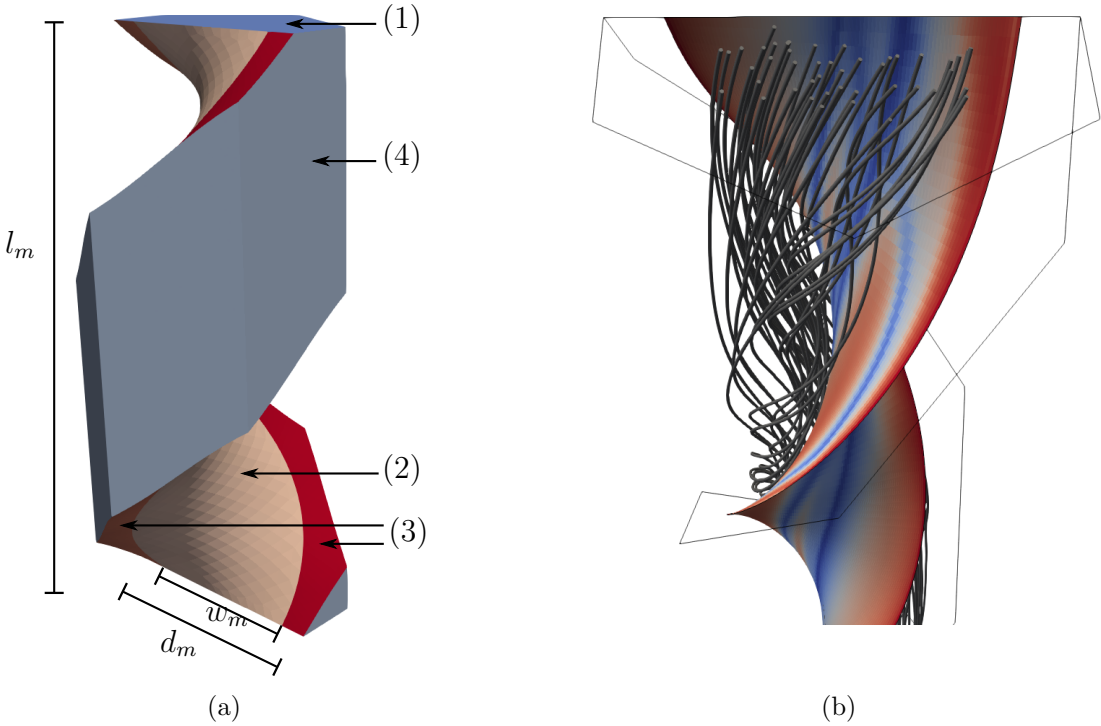


Figure 4.9: (a) Computational domain geometry sketch and boundary condition definition: (1) outlet; (2) membrane; (3) periodic boundaries; (4) symmetry. (b) Local mass transfer on membrane surface and flow streamlines through SHM.

The membrane is modeled as a non-uniform inlet flow field and a non-uniform solute concentration field which are mutually affecting each other. In this study, the feed channel is assumed to have zero solute concentration and insignificant hydraulic pressure. Under these assumptions, the PRO water flux equation (2.15) reduces to:

$$j_w = A \left\{ \frac{\pi_{a,d}}{1 + \frac{B}{j_w} \left[\exp\left(\frac{j_w S}{D}\right) - 1 \right]} - p_d \right\} \quad (4.8)$$

Table 4.3: Geometry and operation parameters for CFD simulations.

| id | $\varepsilon[m^{-1}]$ | w_m/d_m | $l_m[m]$ | $\pi_d[bar]$ | $d_h[m]$ |
|------|-----------------------|-----------|----------|--------------|----------|
| c1 | 0 | 0.75 | 1 | 15 | 0.46 |
| c2 | 0.5 | 0.25 | 2 | 30 | 1.38 |
| c3 | 0.5 | 0.75 | 2 | 15 | 0.46 |
| c4 | 1 | 0.5 | 1 | 30 | 0.68 |
| c5 | 1 | 0.75 | 1 | 15 | 0.45 |
| c6 | 1 | 0.75 | 1 | 30 | 0.45 |

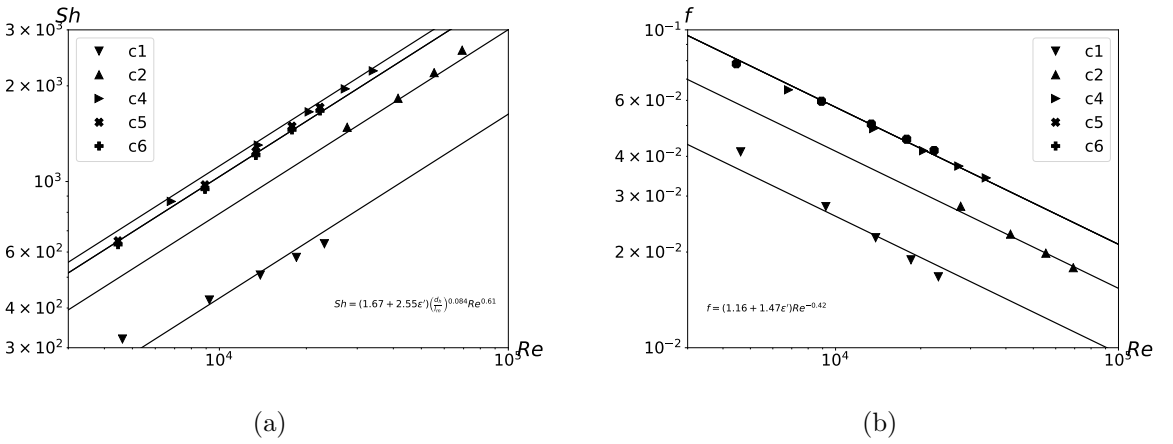


Figure 4.10: (a) Mass transfer characteristics of SHM design: The CFD data series refer to table 4.3. (b) Pressure drop characteristics of SHM design: The CFD data series refer to table 4.3. The data series c5 and c6 are overlapping and appear as disks in the plot.

In order to capture the governing dependencies of the mass transfer coefficient and the pressure drop, the SHM is characterized in terms of scaling laws, against the cross flow U , the twisting rate ε , the membrane width w_m and length l_m , and the draw osmotic pressure π_d . Fig. 4.9(b) shows the membrane boundary with a map of the local mass transfer coefficient, along with streamlines indicating the flow deflection due to the membrane twisting. Table 4.3 summarizes the parameters for the six simulation series. Their results in Fig. 4.10(a) are presented in terms of the Sherwood number $Sh = k_d d_h / D$, against the Reynolds number $Re = U d_h / \nu$. The solid lines represent the least square fit solution, yielding the mass transport scaling relation:

$$Sh = (1.67 + 2.55\varepsilon) \left(\frac{d_h}{l_m} \right)^{0.084} Re^{0.61} \quad (4.9)$$

Similarly, the pressure drop is characterized through the friction number $f = \delta p d_h / (2\rho U^2 l_m)$

Figure 4.10(b) shows the least square fit (4.10).

$$f = (1.16 + 1.47\varepsilon)Re^{-0.42} \quad (4.10)$$

It can be seen that both scaling laws are affected by the membrane twisting ε . It significantly increases both the mass transfer, but also the pressure drop. The non-twisted configuration *c1* however, was not well captured by the scaling laws. A reason for this deviance could be that the flow in *c1* is perfectly laminar, whereas in the other cases, the membrane twisting causes turbulent eddies, and therefore a different scaling behavior.

Operation efficiency analysis

The SHM efficiency is evaluated through a generic mean water flux model, based on the afore-derived mass transfer scaling law: The ECP in the boundary layer can be modeled through the mass transfer coefficient, see **III**:

$$c_{a,d} = \left(c_d + \frac{2B}{\xi A} \right) \exp \left(-\frac{j_w}{k_d} \right) - \frac{2B}{\xi A} \quad (4.11)$$

By substituting equation (4.11) in the water flux equation (4.8), the generic model for the membrane flux, depending on the geometry's mass transfer coefficient, is derived as:

$$J_w = A \left\{ \frac{\left(\pi_d + \frac{2B}{A} \right) \exp \left(-\frac{J_w}{k_d} \right) - \frac{2B}{A}}{1 + \frac{B}{J_w} \left[\exp \left(\frac{J_w S}{D} \right) - 1 \right]} - \frac{\pi_d}{2} \right\} \quad (4.12)$$

The membrane area of one MES is evaluated through the integration of the surface-normal vector in equation (4.13):

$$\begin{aligned} A_m &= 2 \int_0^{l_m} \int_{-w_m/2}^{w_m/2} \|\partial_r \psi \times \partial_z \psi\|_2 \, dr \, dz \\ &= 2l_m \int_{-w_m/2}^{w_m/2} \sqrt{(2\pi\varepsilon r)^2 + 1} \, dr \\ &= l_m \left\{ w_m \sqrt{(\pi\varepsilon w_m)^2 + 1} + \frac{1}{\pi\varepsilon} \ln \left[\pi\varepsilon w_m + \sqrt{(\pi\varepsilon w_m)^2 + 1} \right] \right\}, \end{aligned} \quad (4.13)$$

The permeation flow rate can therefore be written as the product of the permeation flux in equation (4.12) and the membrane surface area in equation (4.13).

In order to analyze the operational efficiency the power gain and consumption is calculated for an SHM system containing 26 MES, with a total membrane surface of

$A_m = 100m^2$, and various recirculation ratios β . Furthermore, an SWM and a PL-FR module with the same membrane are tested under similar operation conditions. For comparison, all configurations are operated with the same system inlet draw flow rate Q'_d which allows to disregard the pressure exchanger and the high pressure pump in this analysis. The net power gain P is therefore defined as the difference between the power generated in the turbine, ΔQp_d , and the energy consumption of the booster pump, $Q_d\delta p/(1-\beta)$. Two draw salt concentrations are considered in this study, which refer to the salinity of seawater and brine. The algorithm for calculating the draw dilution π_d^{eff} is found in **III**. Table 4.4 shows how the recirculation ratio β affects the maximum cross flow velocity through the SHM and the consequent degrees of dilution.

Table 4.4: SHM configurations with different recirculation fractions and resulting cross flow and relative dilution with respect to maximum inflow $Q'_{d,max}$.

| config | β | U_{max} [cm/s] | $\pi_{d,min}^{eff}/27\text{ bar}$ | $\pi_{d,min}^{eff}/54\text{ bar}$ |
|---------|---------|------------------|-----------------------------------|-----------------------------------|
| SHM_1 | 0.98 | 49.9 | 0.93 | 0.92 |
| SHM_2 | 0.97 | 33.2 | 0.93 | 0.92 |
| SHM_3 | 0.9 | 10.0 | 0.94 | 0.93 |
| SHM_4 | 0.0 | 1.0 | 1.0 | 1.0 |

Figure 4.11(a) shows the net power gain in the seawater PRO application ($\pi_d = 27\text{ bar}$) against the system inflow for the SHM with different recirculation ratios, together with the SWM and PL-FR. All configurations exhibit concave graphs which eventually become negative as Q'_d is increased, due to the steep increase in pressure drop for high cross flow velocities. It is also seen that the draw recirculation has a great effect on the net power gain. Considering that the energy consumption of the pressure exchanger and the high pressure pump are neglected, which are proportional to Q'_d , a high recirculation ratio of $\beta > 90\%$ seems reasonable. It is also shown that the more densely packed module types SWM and PL-FR perform worse, which is due to the significantly greater pressure drop in these modules. Figure 4.11(b) shows the net power gain in the brine application with $\pi_d = 54\text{ bar}$. The graphs are quantitatively similar to the seawater case, with greater amplitudes. This is due to greater water fluxes, at similar pressure drops. All configurations are therefore operated more effectively at greater draw concentrations.

The novel SHM design is characterized in terms of mass transfer and pressure drop. The derived power laws quantify the efficiency of the fundamental design aspect of twisted membrane sheets. They effectively reduce ECP and increase the water flux. The subsequent operation efficiency analysis shows that the pressure drop is small compared to densely packed module types, resulting in greater net power generation, if the draw stream is recirculated. Future work on the SHM design will be

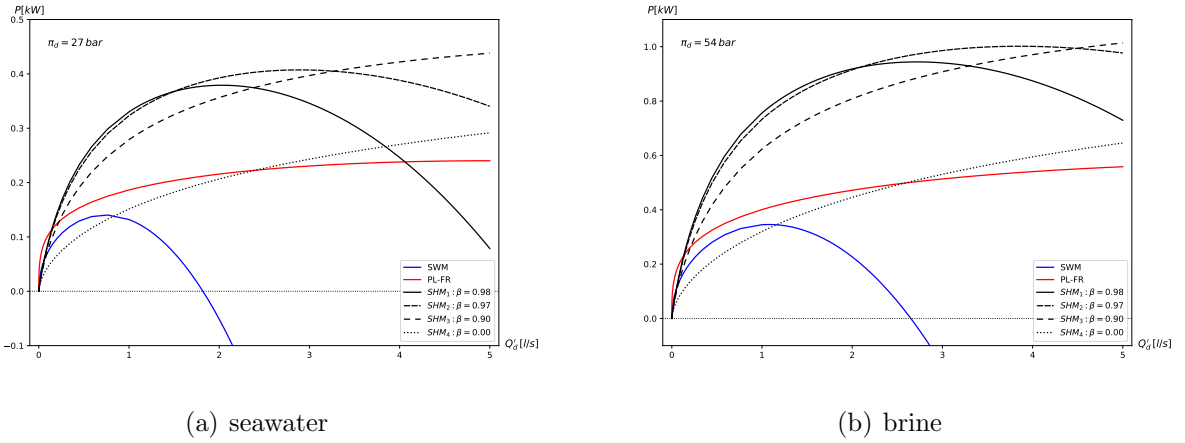


Figure 4.11: Net power gain in PRO against system inflow for SHM systems with various recirculation rates and SWM and PL-FR configurations.

concerned with the development of an experimental prototype validating the effects of membrane twisting, the low packing density, and the draw recirculation.

5 Conclusions & Outlook

Fluid dynamics modeling has been demonstrated to accurately simulate membrane separation processes. Various CFD models were developed and applied for the characterization of membrane module geometries and their optimization. Both, for the well-advanced RO technology, and the advancing ODMPs, the developed models revealed interesting solutions for the technology progress and its efficient operation.

Exhausting Reverse Osmosis Performance

RO technology has matured during decades of research. However, its significant energy demand remains an economic and environmental issue. Making RO desalination more efficient, in terms of energy demand per filtrated volume, was the focus of the first part of this thesis.

Feed spacer optimization in SWM

In the first study on RO, Chpt. 3.1, the filtration process efficiency was quantified through a full characterization of orthogonal feed spacers, in terms of their mass transport- and pressure drop characteristics. Based on these, the filtration efficiency was analyzed for three RO applications, namely brackish water-, seawater-, and brine desalination. It was shown that a 45°-oriented feed spacer significantly improves the filtration efficiency for seawater- and brine desalination, while it is insignificant for brackish water applications. In addition to that, it could be shown that thicker feed spacers improve the filtration rate and lower the pressure drop, which has to be evaluated against the consequently lower membrane packing density. The results of this study allow the application-specific design of SWMs for RO, meeting objective **O1** of this PhD project. Future work on assessing and optimizing RO efficiency through feed spacer characterization will concentrate on the model validation with experimental data, the modification of the CFD algorithm to also include membrane fouling, and the further development of the meshing algorithm to non-orthogonal spacer types.

RO desalination plant design

The OMSD tool was developed for the simulation of full-scale desalination plants. Its application was demonstrated for simulating different desalination designs for brackish water- and brine desalination, outlining the necessity for fundamentally

different design approaches, and revealing favorable designs and corresponding operating conditions. Thereby, this study meets objective **O4** of this PhD project. Further improvements to the RO-efficiency will be yielded by introducing osmosis-driven membrane technologies into the filtration process. Hybrid membrane processes, such as FO-RO or RO-PRO, may significantly decrease the RO energy demand. The implementation of these hybrid processes will allow for the more accurate simulation and efficiency quantification of advanced desalination plants.

Advancing Osmosis-Driven Membrane Technologies

ODMPs show great potential as stand-alone processes, or in combination with RO as hybrid processes. Their efficiency, however, needs to be improved in order to be commercialized in more applications. The second part of this thesis was concerned with the ODMP efficiency improvement through module geometry optimizations.

Packing densities in hollow fiber modules for FO

The third study in this thesis, Chpt. 4.1, was concerned with the design optimization of hollow fiber modules for FO. The permeation flow rate and pressure drop were analyzed for the packing density of the embedded fibers. Through the comparison with experimental data, the simplistic CFD model was shown to accurately predict the water flux for a wide range of draw solute concentrations. Subsequently, it was shown that the total permeation flow rate grows sub-linearly as the packing density is increased. However, the pressure drop was shown to grow exponentially for increasing packing densities. A reasonable compromise between permeation flow and pressure drop was found for a packing density of 0.7. Through the developed CFD model and the derived results, this PhD project's objective **O2** was met. Future work on model refinement will concentrate on replacing the van 't Hoff equation with a more general coupling between solute concentration and osmotic pressure, extending the applicability of this model. Furthermore, the implementation of a membrane fouling model will allow for the simulation of operation cycles. Finally, the computational domain will be modified to simulate the effect of non-hexagonally, chaotically packed fibers.

The characterization of a novel, PRO-specific module type

In the last study, a novel module design for PRO, the SHM, was suggested. Its fundamental design features are the helically-twisted membrane sheets and the consequent low packing density. The helical membrane sheets were shown to effectively mix the draw solution, reduce ECP, and increase the power density. Due to the low membrane packing, the pressure drop through the module is low, increasing the net

energy generation. The PRO design performance was evaluated against two traditional filtration module designs, for applications with seawater and brines as draw streams, indicating a superior efficiency of the SHM module design. This study meets objective **O3**, but will be continued in order to prove the benefit of the SHM design: An experimental prototype will be developed providing evidence for the SHM's key-design features, supporting the ongoing patent process.

Bibliography

- Aschmoneit, F. (2018). Scalar surface normal gradient of sources. <https://gitlab.gbar.dtu.dk/fyna/wallNormalScalarGrad.git>. Accessed: 30 December 2019.
- Aschmoneit, F. (2019a). Feed spacer cfd example case. <https://gitlab.gbar.dtu.dk/fyna/ambrosia-diamondBaseCase.git>. Accessed: 30 December 2019.
- Aschmoneit, F. (2019b). Hollow fiber module cfd example case. <https://gitlab.gbar.dtu.dk/fyna/HFM.git>. Accessed: 16 January 2020.
- Aschmoneit, F. (2019c). Omsd repository. <https://github.com/FynnAschmoneit/OMSD>. Accessed: 05 January 2020.
- Aschmoneit, F. (2019d). Shm repository. <https://gitlab.gbar.dtu.dk/fyna/proHelixDev.git>. Accessed: 08 January 2020.
- Box, G. E. P. (1976). Science and statistics. *Journal of the American Statistical Association*, 71(356), 791–799.
- Dalin, C., Wada, Y., Kastner, T., & Puma, M. J. (2017). Groundwater depletion embedded in international food trade. *Nature*, 543(7647), 700–704. doi:10.1038/nature21403
- Dow(Du Pont). (2019). ROSA/WAVE. Retrieved from <https://www.dupont.com/water/design-software.html>
- Gu, B., Adjiman, C. S., & Xu, X. Y. (2017). The effect of feed spacer geometry on membrane performance and concentration polarisation based on 3D CFD simulations. *Journal of Membrane Science*, 527, 78–91. doi:10.1016/j.memsci.2016.12.058
- Günther, J., Schmitz, P., Albasi, C., & Lafforgue, C. (2010). The effect of feed spacer geometry on membrane performance and concentration polarisation based on 3d cfd simulations. *Journal of Membrane Science*, 348, 277–286. doi:10.1016/j.memsci.2009.11.011
- Kaçaroğlu, F. (1999). Review of groundwater pollution and protection in karst areas. *Water, Air, and Soil Pollution*, 113(1), 337–356. doi:10.1023/A:1005014532330
- Karabelas, A., Kostoglu, M., & Koustou, C. (2015). Modeling of spiral wound membrane desalination modules and plants - a review and reserach priorities. *Desalination*, 356.
- Landau, L. & Lifshitz, E. (1987). *Fluid Mechanics, Course of Theoretical Physics* (2nd ed.). Elsevier.
- Lau, K. K., Abu Bakar, M. Z., Ahmad, A. L., & Murugesan, T. (2009). Feed spacer mesh angle: 3D modeling, simulation and optimization based on unsteady hydrodynamic in spiral wound membrane channel. *Journal of Membrane Science*, 343, 16–33. doi:10.1016/j.memsci.2009.07.001

- Lee, K. L., Baker, R. W., & Lonsdale, H. K. (1981). Membranes for power generation by pressure-retarded osmosis. *Journal of Membrane Science*, 8(2), 141–171. doi:10.1016/S0376-7388(00)82088-8
- Loeb, S., Titelman, L., Korngold, E., & Freiman, J. (1997). *Effect of porous support fabric on osmosis through a Loeb-Sourirajan type asymmetric membrane*.
- Meister, A. (2015). *Numerik linearer gleichungssysteme*. Springer.
- MEMENTO. (2019). <http://www.memento.env.dtu.dk/project-overview>. Accessed: 25 December 2019.
- Moukalled, F., Mangani, L., & Darwish, M. (2016). *The finite volume method in computational fluid dynamics*. Springer.
- Mulder, M. (1991). *Basic principles on membrane technology*. Springer Netherlands.
- Patankar, S. (1980). *Numerical heat transfer and fluid flow*. Hemisphere Publishing Corporation.
- Ren, J. & Mccutcheon, J. R. (2017). Making Thin Film Composite Hollow Fiber Forward Osmosis Membranes at the Module Scale Using Commercial Ultrafiltration Membranes. *Industrial & Engineering Chemistry Research*, 56. doi:10.1021/acs.iecr.6b04931
- Schock, G. (1987). Mass transfer and pressure loss in spiral wound modules. *Desalination*, 64, 339–352.
- Schwarzenbach, R. P., Egli, T., Hofstetter, T. B., von Gunten, U., & Wehrli, B. (2010). Global water pollution and human health. *Annual Review of Environment and Resources*, 35, 109–136.
- Semiat, R. (2008). Energy issues in desalination processes. *Environmental Science & Technology*, 42(22), 8193–8201. doi:10.1021/es801330u
- Significant Desalination Market Points. (2013). <https://yatesenvironmentalservices.wordpress.com/category/desalination/>. Accessed: 29 December 2019.
- SUEZ Water Technologies and Solutions. (2019). Winflows. Retrieved from <https://www.suezwatertechnologies.com/resources/winflows>
- Sustainable Development Goals. (2015). <http://www.un.org/sustainabledevelopment/>. Accessed: Web.11 May 2017.
- The OpenFOAM Foundation. (2018). *Openfoam v6 user guide*. Retrieved from <https://cfd.direct/openfoam/user-guide>
- The United Nations World Water Development Report. (2019). <https://www.unwater.org/publications/world-water-development-report-2019/>.
- Toray. (2019). Toray DS. Retrieved from <https://ap3.toray.co.jp/toraywater/>